STARS

Electronic Theses and Dissertations, 2004-2019

2005

Instrumented Nanoindentation Studies Of Deformation In Shape Memory Alloys

Sudhir Rajagopalan
University of Central Florida

Part of the Materials Science and Engineering Commons

Find similar works at: https://stars.library.ucf.edu/etd

University of Central Florida Libraries http://library.ucf.edu

Showcase of Text, Archives, Research & Scholarship

INSTRUMENTED NANOINDENTATION STUDIES OF DEFORMATION IN SHAPE MEMORY ALLOYS

by

SUDHIR RAJAGOPALAN

B.S. Regional Engineering College, Rourkela, 1996
M.S. University of Central Florida, Orlando, 2003

A dissertation submitted in partial fulfillment of the requirements
for the degree of Doctor of Philosophy
in the Department of Mechanical Materials and Aerospace Engineering
in the College of Engineering and Computer Science
at the University of Central Florida
Orlando, Florida

Summer Term
2005

Major Professor: Dr. Rajan Vaidyanathan

ABSTRACT

Near equi-atomic nickel titanium (NiTi) shape memory alloys (SMAs) are a class of materials characterized by their unique deformation behavior. In these alloys, deformation mechanisms such as mechanical twinning and stress induced phase transformation between a high symmetry phase (austenite) and a low symmetry phase (martensite) additionally occur and influence mechanical behavior and thus their functionality. Consequently, applications of SMAs usually call for precise phase transformation temperatures, which depend on the thermomechanical history and the composition of the alloy. Instrumented indentation, inherently a mechanical characterization technique for small sampling volumes, offers a cost effective means of empirically testing SMAs in the form of centimeter scaled buttons prior to large-scale production. Additionally, it is an effective probe for intricate SMA geometries (e.g., in medical stents, valves etc.), not immediately amenable to conventional mechanical testing.

The objective of this work was to study the deformation behavior of NiTi SMAs using instrumented indentation. This involved devising compliance calibration techniques to account for instrument deformation and designing spherical diamond indenters. Substantial quantitative information related to the deformation behavior of the shape memory and superelastic NiTi was obtained for the first time, as opposed to existing qualitative indentation studies.

For the case of shape memory NiTi, the elastic modulus of the B19' martensite prior to twinning was determined using spherical indentation to be about 101 GPa, which was comparable to the value from neutron diffraction and was substantially higher than typical values reported from extensometry (68 GPa in this case). Twinning at low stresses was observed from neutron

iii

diffraction measurements and was attributed to reducing the elastic modulus estimated by extensometry. The onset of predominantly elastic deformation of the twinned martensite was identified from the nanoindentation response and the elastic modulus of the twinned martensite was estimated to be about 17 GPa. Finite element modeling was used to validate the measurements.

For the case of the superelastic NiTi, the elastic modulus of the parent austenite was estimated to be about 62 GPa. The onset of large-scale stress induced martensite transformation and its subsequent elastic deformation were identified from the nanoindentation response. The effect of cycling on the mechanical behavior of the NiTi specimen was studied by repeatedly indenting at the same location. An increase in the elastic modulus value for the austenite and a decrease in the associated hysteresis and residual depth after the initial few cycles followed by stabilization were observed. As for the case of shape memory NiTi, finite element modeling was used to validate the measurements.

This work has initiated a methodology for the quantitative evaluation of shape memory and superelastic NiTi alloys with instrumented spherical indentation. The aforementioned results have immediate implications for optimizing thermomechanical processing parameters in prototype button melts and for the mechanical characterization of intricate SMA geometries (e.g., in medical stents, valves etc.)

ACKNOWLEDGMENTS

Assistance given by those who ne'er received our aid is debt by gift of heaven and earth but poorly paid

(Translated from Tamil)

Thiruvalluvar, tamil philosopher, in Thirukurral, 1st Century B.C.

TABLE OF CONTENTS

LIST OF FIGURES

1. INTRODUCTION

1.1 <u>Motivation</u>

NiTi SMAs are characterized by their unique mechanical behavior, where the stress strain response of the material is influenced by events such as twinning and phase transformations which, consequently, affects their functionality. In the case of Ti rich alloys (shape memory NiTi) these phase transformations are thermally driven (at room temperatures) and in Ni rich alloys (superelastic NiTi) these are driven by stress (at room temperatures). These transformations and thereby the mechanical behavior are extremely sensitive to the chemical composition of the alloys. Consequently, alloy development for commercial purposes or otherwise, involves fabrication of alloys with varying compositions and in relatively larger sizes for macro scale mechanical testing, which renders the whole process very cost intensive. Instrumented indentation is an established technique of extracting mechanical properties from small volume samples and structures and offers a cost effective means of optimizing thermo-mechanical processing parameters prior to large-scale production. Additionally, it is an effective probe for intricate SMA geometries (e.g., in medical stents, valves etc.), not immediately amenable to conventional mechanical testing. However, while the deformation behavior of NiTi materials on a macro scale has been studied extensively by the scientific community, a comprehensive methodology for property extraction using instrumented nanoindentation in these materials is lacking.

While the primary objective of this work was to study the deformation behavior of NiTi SMAs using instrumented nanoindentation, it was also an attempt to establish a comprehesive

methodology for property extraction using spherical indentation for the case of SMAs. The installation and commissioning of an instrumented nanoindenter at the Advanced Materials Processing and Analysis Center (AMPAC), UCF as part of the author's master's thesis laid the groundwork for this doctoral research.

1.2 <u>Organization</u>

As mentioned earlier, this work advanced the work accomplished at the master's level to the next stage. While, the primary focus of the master's thesis was to install and commission the instrumented nanoindenter and tailor it to suit the local needs and NiTi SMAs, the current work began with designing diamond spherical indenters and establishing the compliance calibration technique. While these and other issues such as the rationale behind using spherical indenters are discussed along with nanoindentation studies on shape memory and superelastic NiTi in subsequent chapters, an overview of instrumented indentation has been detailed in <u>chapter 2</u> and ref. 1.

<u>Chapter 3</u> provides a brief introduction to NiTi shape memory alloys and their macroscopic mechanical behavior. Objective of this work has been further discussed in ref. 2.

<u>Chapter 4</u> details the study of elastic behavior of shape memory NiTi using instrumented indentation and compares the findings with those from conventional extensometry and *in situ* neutron diffraction. This section of the work was published in ref. 3.

In Chapter 5, deformation behavior of the shape memory NiTi beyond elasticity is described. Additionally, spherical indentation results are contrasted with sharp indentation. Finite element modeling was employed to validate the results. This work is the first of a two part series to be submitted for publication[4].

Chapter 6 details instrumented indentation studies on superelastic NiTi. Effect of cycling on the nanoindentation response of superelastic NiTi has been studied using nanoindentation. Sharp indentation results from superelastic NiTi have also been presented. The initial studies on superelastic NiTi using indentation were published as ref. 2 and the recent work presented here is being prepared for publication as the second of the two part series mentioned earlier[5].

In Chapter 7, the variation in mechanical properties with carbon nanotubes content in a carbon nanotube reinforced polymer derived ceramic composite is studied. This also serves as an example of how the spherical indentation and the calibration methodology developed above can be extended to other material classes. This work was published as ref. 6.

Finally, chapter 8 details the overall conclusions from this work and lists directions in which this work can be extended to in the future.

2. INSTRUMENTED INDENTATION

This chapter reviews instrumented indentation as a qualitative and quantitative mechanical characterization technique that is applicable to nano- and microscale volumes and structures. Existing methodologies for estimating elasto-plastic properties from representative load-depth data are briefly reviewed and the principle behind such approaches is emphasized. Selected examples are also presented to illustrate the applicability of nanoindentation to a variety of material classes and geometries.

2.1 <u>Introduction</u>

Instrumented indentation or generally referred to as nanoindentation, when conducted on a sub-micron regime, primarily consists of a controlled load (P) applied through a diamond tip that is in contact with a specimen. The penetration depth (h) of the tip into the material is recorded as a function of the applied load. A typical nanoindenter can record depths to sub-nanometer and loads to sub-mN resolution, respectively. From the recorded load (P)-depth (h) response, various characteristic mechanical properties such as Young's modulus, strain-hardening exponent, fracture toughness, etc., can be estimated.

A hard indenter, usually a diamond, transfers the load on to the material and makes an impression. The analysis of the depth of the impression in conjunction with the loading characteristics, is used to determine the mechanical properties. Indenters may be sharp (e.g., Berkovich, Vickers, cube corner, etc.), spherical or even flat-ended cylindrical punches. More details about indenters are given in a following section.

Advantages of nanoindentation are-

It is a convenient tool for mechanical characterization related to the performance and reliability of small-volume structures (e.g., thin films for microelectronic/optoelectronic devices, surface coatings for optical, magnetic, thermal, environmental and tribological performances). Conventional testing methods such as tensile testing cannot be easily used to obtain mechanical properties at these size scales. Often times this need for small scale mechanical characterization is not merely limited to cases involving mechanical functionality, but extends to applications where functionality is coupled with mechanical behavior (e.g., assessing the thermo-mechanical reliability of patterned Cu or Al interconnect lines in microprocessors). It requires small sampling volumes and consequently can be used to test materials not immediately available in bulk volumes. Examples include amorphous metals or metallic glasses that are not amenable to fabrication in large quantities due to the difficulties associated with suppressing crystallization, or shape-memory alloys with controlled transformation temperatures that are typically fabricated as prototype button-melts to save costs prior to large-scale production. It is a technique that can be used over multiple length scales, i.e., nano-, micro- and macroscales, by simply varying the geometry and penetration depth of the indenter. It probes the multiaxial deformation characteristics of a material, given that the stress state under an indenter is inherently multiaxial.

A hard indenter, usually a diamond, transfers the load on to the material and makes an impression. The analysis of the depth of the impression, in conjunction with the loading characteristics, is used to determine the mechanical properties. Indenters may be sharp (e.g., Berkovich (figure 2-1a, Vickers, cube corner, etc.), spherical (figure 2-1b) or even flat-ended cylindrical punches. Spherical indenters may be preferred over sharp indenters owing to the non-

singular nature of the stress fields below the indenter and additionally, due to the concomitant restraint they impose on damage and plasticity. This means that the onset of plasticity upon indentation is delayed when a spherical indenter is employed. However, this becomes a hindrance to the application of nanoindentation in assessing the properties of thin films or small volumes of material, where the large indent size cannot be physically accommodated due to geometrical constraints. By contrast, sharp indenters induce plastic deformation at an earlier stage during loading and hence are more amenable to nano- and microscale measurements. Furthermore, it is easier to fabricate a faceted diamond indenter rather than a spherical one.

2.2 <u>Extraction of Elasto-Plastic Properties using Sharp Indentation</u>

The load (P) vs. depth (h) data recorded by a typical nanoindenter is represented (for a sharp indenter) in figure 2-2. AB represents the loading and BC the unloading. Loading probes both elastic and plastic deformation of the material while the unloading part of the curve primarily represents the elastic recovery.

During elastic loading, the curve follows the relation $P = Ch^2$, where C can be determined for a sharp Berkovich indenter from

$$P = Ch^2 = 2.189(1 - 0.21v_m - 0.01v_m^2 - 0.41v_m^3)E^*h^2 \qquad \text{2-1}$$

with

$$E^* = \left(\frac{1 - v_1^2}{E_1} + \frac{1 - v_2^2}{E_2} \right)^{-1} \qquad \text{2-2}$$

and representing a reduced modulus that accounts for non-rigid indenters[7]. E_1 and v_1 represent the elastic modulus and the Poisson's ratio of the indenter, respectively, while E_2 and v_2 represent the elastic modulus and the Poisson's ratio of the indented material, respectively.

In principle, extraction of mechanical properties from nanoindentation data requires quantitative analysis of the aforementioned load-depth (P-h) curve. By recourse to analytical, experimental and computational techniques, a variety of methods have been proposed for sharp indentation[8-10]. Some of the more popular techniques for extraction of elasto-plastic properties are those proposed by Doerner and Nix[8], Oliver and Pharr[9] and Suresh and co-workers[10]. For example, Doerner & Nix have expressed the Young's modulus as a function of elastic displacements, obtained from the slope of the unloading curve. This technique relies on the assumption that the area of contact made by the indenter during initial unloading is constant, i.e., the unloading is linear. For determining hardness, the technique does not rely on visual inspections of the indents, but rather uses the plastic depth to determine the indenter contact area. The hardness, H, is then calculated from

$$H = \frac{P_{max}}{A} \qquad\qquad 2\text{-}3$$

where P_{max} is the peak indentation load and A is the area of contact. Hence, knowledge of the exact shape of the pyramidal diamond indenter is essential to the determination of the projected contact area and consequently to the determination of both plastic and elastic properties. The indenter shape is calibrated by making two-stage carbon replicas of indentations in a soft material followed by TEM imaging.

An analysis procedure proposed by Oliver & Pharr differs from the preceding one in that it does not assume unloading to be linear. The elastic properties are still determined from the unloading portion of the curve. The unloading curve is described by a power law that relates the unloading load to the indentation depth, and the slope at the peak load is obtained by analytical differentiation of this relation. The reduced modulus, E* (see equation 2-2) is then determined from this slope and the projected area of elastic contact. In this method, the contact area is not determined by imaging indentations but from an area function that is a result of an iterative procedure, from a series of experimental measurements that also takes the load frame compliance into account.

The approach proposed by Suresh and co-workers uses finite element methods and dimensional analysis to develop functions that relate indentation data to the elasto-plastic properties of the material. The method offers both a "forward" and a "reverse" analysis. The forward analysis predicts a unique indentation response for a given set of elasto-plastic properties, while the reverse analysis determines the elasto-plastic properties from the indentation data. The method recognizes the fact that the load P may be expressed as

$$P = P(h, E^*, \sigma_y, n)$$ 2-4

where h is the depth, E* is the reduced modulus from equation 2-2, σ_y is the yield stress and n is the strain hardening exponent. The exact relations are derived computationally. A key feature of the above method is that it provides unique correlations between the penetration depth and true contact area for commercially available sharp indenters. Thus the need for visual or experimental determination of the contact area is circumvented while still taking into account pile-up and sink-in phenomena. Pile-up, usually observed in low-strain-hardening alloys, refers to the pushing out

of plastically displaced material to the faces of the indenter due to the incompressibility of plastic flow. Sink-in, usually observed in high-strain-hardening alloys, refers to the plastically displaced material pushing away from the faces of indenter with the imprint sinking below the initial surface level.

2.3   Property Extraction by Spherical Indentation

Similarly for a spherical indenter, a general theoretical framework proposed by Suresh and co-workers[11], is an extension of the original formulation derived by Hertz[12], which essentially examines the elastic contact between two spherical solids. In the case of load-depth or P-h measurements one of the surfaces is flat (an infinite radius of curvature) and when the flat surface is indented it has been shown that

$$P = Ch^{3/2} \hspace{6cm} \text{2-5}$$

Where $C = \dfrac{2\sqrt{2}}{3} E^* D^{1/2}$ \hspace{5cm} 2-6

With D as the indenter diameter and with E* representing the reduced modulus as discussed earlier.

The load-depth (P-h) response of a material, subjected to spherical indentation, essentially contains the initial elastic portion (in the loading portion of the curve) that follows the above-mentioned Hertzian law. So, a 3/2 power fit to the initial portion of the P-h curve gives a value for the constant C and the elastic modulus can be derived using the relation from equation 2-6. Also, any deviation from this slope of 3/2 on a log P vs. log h plot indicates a deviation from the

elastic behavior which could be because of either the onset of plastic deformation or in the case of SMAs due to any of the phenomenon like phase transformations or twinning.

Among the plastic properties, the strain hardening exponent, n, can be estimated from the slope of a linear fit to the plastic portion of the log P vs. log h curve. This follows from the relations proposed by Meyer[11], Tabor[13] and the experimental results of Norbury and Samuels[14].
Meyer derived the empirical relation

$$P = \frac{Ka^m}{D^{m-2}} \qquad \text{2-7}$$

where P is the load, D is the indenter's diameter, a is the contact radius of the indent and K is a material constant. Tabor proposed that the stress-strain curve of a metal can be characterized by

$$\sigma = \sigma_0 \varepsilon^n \qquad \text{2-8}$$

where ε is the plastic strain, σ_0 is the stress when ε is 1.0 and n the strain hardening exponent and showed that

$$m = n + 2 \qquad \text{2-9}$$

Norbury and Samuels showed that a numerical constant c can be derived which measures the sinking-in or piling-up at the perimeter of the contact area and is given by

$$c^2 = \frac{a^2}{Dh} \qquad \text{2-10}$$

where a is the contact radius and h the depth of penetration of the indenter.
from equations 2-7 to 2-10, it follows that

$$P \propto h^{1+\frac{n}{2}} \qquad \text{2-11}$$

and hence n, can be calculated from the slope of a linear fit to the plastic portion of the log P vs. log h curve.

2.4   **Other Properties**

In addition to some of the properties discussed in the preceding section, creep, residual stresses, fracture toughness etc., have also been estimated using nanoindentation. A method proposed by Hardings, Oliver and Pharr[15] to estimate fracture toughness of brittle materials is based on radial cracks that are generated in a brittle material when subjected to sharp indentation. The length of these radial cracks, c, is related to the fracture toughness of the material, K_c, through:

$$K_C = \alpha \left(\frac{E}{H} \right)^{\frac{1}{2}} \left(\frac{P}{c^{\frac{3}{2}}} \right) \qquad\qquad 2\text{-}12$$

where P is the peak load, E is the material's elastic modulus, H is its hardness and α is an empirical constant that depends on the indenter geometry. With significant improvement in instrumentation associated with nanoindentation, strain rate sensitivities (analogous to creep testing in uniaxial tension) have been determined during an indentation test. Mayo & Nix[16] have proposed a constant rate of loading test that can obtain such data from indentation tests. Suresh & Giannakopoulos[17] have also proposed a new method for estimating residual stresses by instrumented sharp indentation. They expect the technique to have direct uses for residual stress measurements in such applications as thin films for microelectronics and optoelectronics, structural coatings, and engineered surfaces whose properties are altered by such methods as mechanical working, etching, ion implantation, case hardening, laser treatments, shot peening or laser shock peening. The indentation response (i.e., the P-h curve) of a stress-free material is compared to the one obtained from the same material having residual stresses. Data from both

these responses are used to quantitatively determine the residual stresses. The aforementioned examples have outlined methodologies for the quantitative determination of mechanical properties from indentation data. Indentation can also serve as a qualitative probe to examine materials phenomena and functionality at nano- and microscales. The following selected examples highlight the versatility of indentation in examining scientific (e.g., dislocation nucleation) and engineering (e.g., toughness and yield criterion) issues in a variety of materials (e.g., functionally-graded WC-Co, amorphous metals and Al thin films).

Example - Hardness and Toughness of Functionally-Graded WC-Co

Indentation over nano- and microscales has been used to determine the hardness and toughness of functionally graded WC-Co materials that find application as tool-bits[18]. The materials had continuous compositional gradients to within about 40 microns below the surface. Hardness measurements were made as a function of depth in the graded zone i.e., 40 microns. The hardness was correlated with composition and complimentary x-ray diffraction measurements that estimated the residual stresses. Quantitative estimates of the toughness were obtained using the approach previously described in this article. Qualitatively, improved toughness was observed in the functionally-graded material when compared to an equivalent homogenous specimen. This is shown in figure 2-3 where identical tests were performed in the graded and the homogenous material. Cracks radiate in the homogenous sample, while not immediately apparent in the functionally-graded materials. Such investigations can be used to establish optimal gradients in order to enhance tool-bit life.

Example - Bulk Metallic Glasses

Deformation in metallic glasses occurs inhomogeneously and is concentrated in localized shear bands. There is no large-scale plasticity when a dominant shear band propagates through a test specimen. However, testing in constrained geometries generates multiple shear bands, which are associated with large-scale plasticity and elastic-perfectly-plastic deformation. Instrumented indentation is particularly suited to investigating metallic glasses since the plastically deformed volume under the indenter is confined by the surrounding undeformed material, thereby restricting the unstable propagation of shear bands. The resulting multiaxial state of stress under an indenter facilitates the determination of yield criteria under such loading conditions.

Instrumented sharp indentation experiments at the nano- and micro-length scales were carried out in an attempt to quantify the deformation characteristics of a $Zr_{41.25}Ti_{13.75}Cu_{12.5}Ni_{10}Be_{22.5}$ bulk metallic glass[19]. The experiments were accompanied by detailed three-dimensional finite element simulations of instrumented indentation to formulate an overall constitutive response. By matching the experimentally observed continuous indentation results with the finite element predictions, a general Mohr-Coulomb type constitutive description was extracted to capture the dependence of multiaxial deformation on both shear stresses and normal stresses. This constitutive response is able to provide accurate predictions of the evolution of shear bands seen in uniaxial compression tests. Constrained deformation of the material around the indenter results in incomplete circular patterns of shear bands whose location, shape and size are also captured well by the numerical simulations. The analysis is also able to predict the extent of material pile-up observed around the indenter. The surface deformation features are also

consistent with mechanisms such as localized shear flow, serrated yielding and adiabatic heating, which are observed during macroscopic mechanical tests.

Figure 2-4a shows the load-depth nano indentation response of metallic glass. The solid line is the expected behavior predicted from finite element simulations using a Mohr-Coulomb yield criterion while the dashed line is the expected behavior predicted using a von Mises yield criterion. Previously, the yield criterion had been unresolved from conventional mechanical tests and this work has assisted in resolving some of those issues. Also shown in figure 2-4b is the indented surface with characteristic incomplete circular patterns, which are also captured well in the finite element simulations in figure 2-4c.

Example - Thin Films

While nanoindentation is an efficient tool that can be employed to extract the mechanical properties of thin films, an understanding of discreet and continuous deformation associated with nanoindentation of thin films is essential to gauge the size dependence of plastic properties, besides possible insights into the micro-mechanisms of plasticity. Gouldstone et al[20] used nanoindentation to investigate this phenomenon in both polycrystalline and single crystal Al thin films. The samples exhibited displacement bursts or jumps at constant loads in the load-depth response as shown in figure 2-5a. The pressure under the indenter tip at which the first bursts are generated were correlated with the theoretical shear strength of the thin film. The authors postulate that the displacement bursts induced in the thin films by nanoindentation are primarily a consequence of the punching of geometrically necessary dislocations. A simple energetics model is proposed that obtains the elastic energy from the area under the nanoindentation load-

depth curve and relates this to the energy necessary for punching out dislocations. The authors also use transmission electron microscopy to show arrays of dislocations that are punched out within grains surrounding the indentation (figure 5b).

2.5 <u>Conclusion</u>

Instrumented indentation relies on robust analysis of reliable load-depth (P-h) data for the quantitative determination of mechanical properties. This is perhaps the primary limitation. While significant progress has been made in eliminating the need for visual inspection of indents, which is subject to human interpretation, a comprehensive theoretical framework that can be used for extracting elasto-plastic properties of a variety of materials classes is still elusive. Given the complexity of constitutive response to the multi-axial loading states under an indenter such a framework is perhaps possible through the combined use of analytical, experimental and computational techniques. The work on amorphous alloys presented in this chapter illustrates this point - instrumented indentation in combination with finite element methods was able to establish that the alloy investigated follows a Mohr-Coulomb yield criterion rather than a von Mises criterion.

Instrumented indentation over nano- and microscales is rapidly emerging as an effective and versatile tool for qualitative and quantitative mechanical characterization of small volumes. Progress in instrumentation and metrology at these size scales, along with significant advances in atomic-scale characterization, continues to provide the technique with impetus for rapid growth. Concomitant with this increase in the resolution and reliability of instrumented indentation data, data analysis methodologies continue to be developed for accurate property determination.

2.6 **Figures**

1.0

60°

65.3°

5.02

2.03

5.0 R

(a) Berkovich Indeter

(b) A typical stainless steel spherical indenter used on the Nanotest-600 Dimensions in millimeters
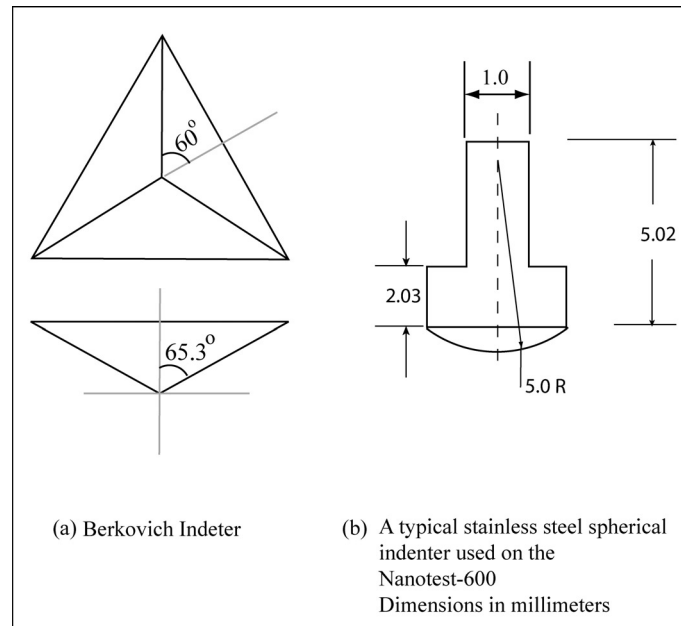
Figure 2-1: (a) a standard Berkovich indenter (b) a typical spherical indenter.

P

P

P (load)

Loading

Unloading

B

A   h (depth)   C

MECHANICAL PROPERTIES OF NANO- AND MACROSCALE VOLUMES AND STRUCTURES
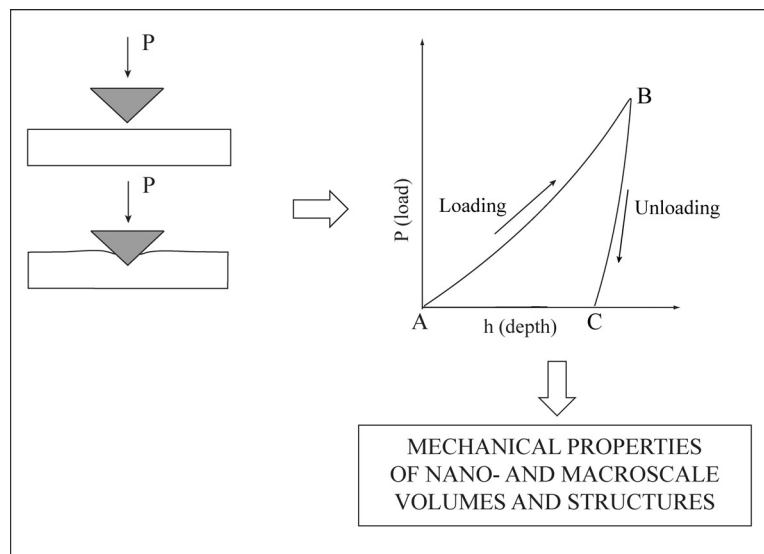
Figure 2-2: A schematic of instrumented indentation.
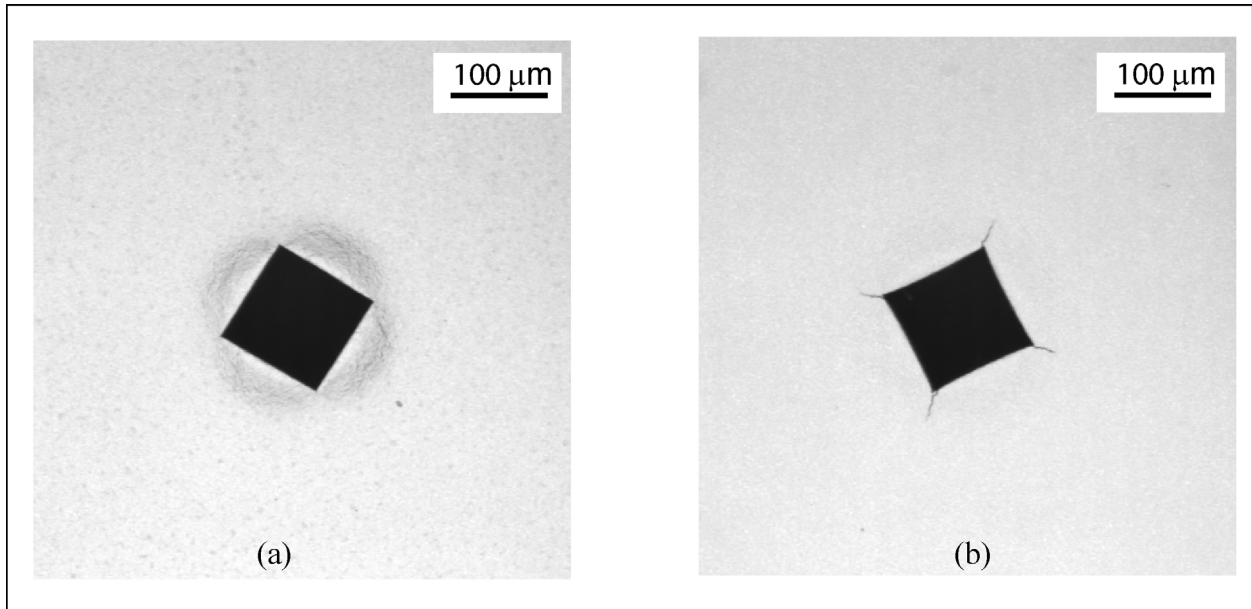
Figure 2-3: Microindents in (a) functionally graded WC-Co and (b) an equivalent homogenous WC-Co specimen, showing improved toughness in the former as indicated by the absence of cracks[18].
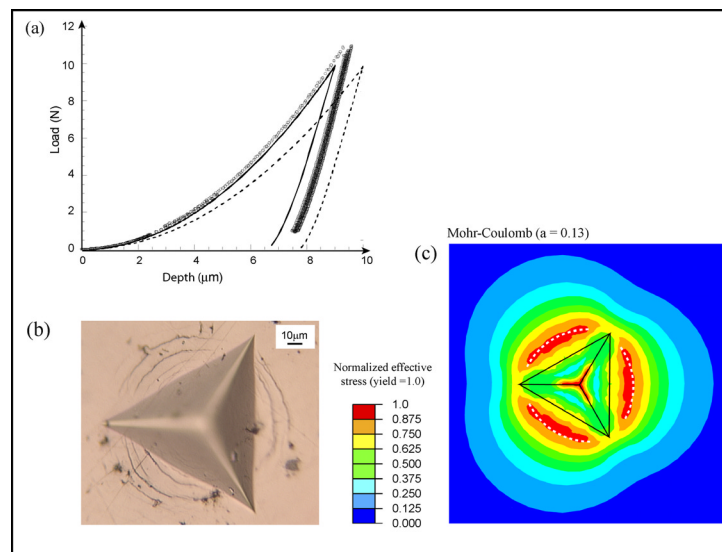
Figure 2-4: (a) Indentation response of metallic glass during loading and unloading. The solid line is a finite element simulation using a Mohr-Coulomb yield criterion while the dotted line uses a von Mises yield criterion. (b) Optical micrograph of a 9 micron deep Berkovich indent showing characteristic patterns upon unloading which are captured in (c) the finite element simulation[19].
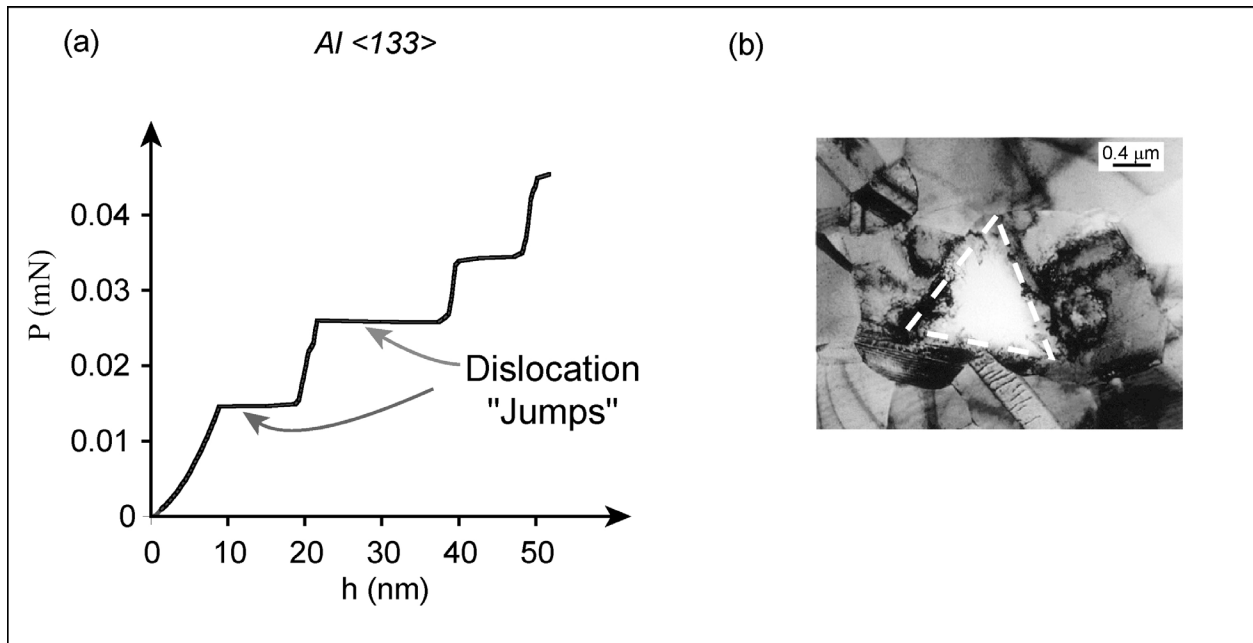
Figure 2-5: (a) Nanoindentation response from a (133) orientated, 400 nm thick, single crystal Al film. The bursts are attributed to dislocation activity. (b) Such activity is captured in this TEM image of a Cu film, which shows dislocations that are punched out within a grain around an indent[20].

3. SHAPE MEMORY ALLOYS

The shape memory effect was first discovered in the 1930s and the first reported observation of the shape memory effect was by Chang and Read[21] in the AuCd system. This effect was observed in the NiTi system in 1962 by Buhler and co-workers[22] at the U.S Naval Ordinance Laboratory and hence the alloy was named Nitinol. Since then shape memory alloys have been the subject of intense research and have been developed as an important class of materials with wide applications. In this chapter, a brief overview of the shape memory alloys, their unique mechanical behavior and their applications is presented.

3.1 The Shape Memory Effect and Superelasticity

The shape memory effect (SME) refers basically to the ability certain materials exhibit wherein they "remember" and are able to recover their pre-set shapes even after severe deformation. The driving force behind such behavior is a martensite transformation and the ability of these materials to transform from and to martensite. Martensite transformation is a first order displacive transformation generally associated with steel, and details of martensite transformation can be found elsewhere[23-25]. In the case of SMAs this martensite transformation is thermo-elastic and takes place over a very small temperature range. SMAs transform in to the martensite phase when cooled below a critical temperature called the martensite start temperature, M_s. However, this transformation is not over at the M_s temperature but extends over a temperature range below M_s and ends at what is called as the martensite finish temperature or M_f. The alloy is said to be now in the martensitic state. When the alloy is heated after being deformed in its martensitic state, the strains induced and thus the original shape are completely

recovered as the martensite is transformed to austenite, the parent phase. This transformation starts at the austenite start temperature or A_s and ends at A_f or the austenite finish temperature. There is a hysteresis associated with this first order transformation between the low temperature martensite and the high temperature austenite. The transformation temperatures are unique to a particular alloy and depend on factors like alloy composition and thermomechanical processing. A schematic of the hysteresis associated with the aforementioned transformation is depicted in figure 3-1.

The above-discussed phenomenon is what is called the one-way shape memory effect, where the SMA regains its shape after being heated to the austenite phase. For the next cycle the SMA has to be cooled back to the martensite phase. SMAs can exhibit even two-way shape memory, where they can regain their shapes in the two phases upon heating and cooling, spontaneously. However for the two way shape memory effect substantial biasing of the martensite phase is required where the number of variants of martensite that form upon transformation is limited.

The origin of the shape memory effect is closely related to the very nature of the martensite and austenite phases[26]. Martensite is a lower symmetry phase than the austenite. Consequently, transformation to martensite results in the formation of randomly oriented variants. When this martensite is deformed the twin boundaries migrate resulting in a biased distribution of the variants. However upon heating either the deformed or the undeformed martensite, both, result in a reversion to the austenite phase and thus recovery of the original shape, as only one reverted structure is possible. This simple concept lies behind the shape memory effect and is schematically shown in figure 3-2.

Also associated with SMAs is a phenomenon called superelasticity, where the martensite formation is stress-induced unlike what was discussed in the previous section. Application of stress above the M_s temperature (essentially the austenite phase) results in the formation of martensite, known as stress-induced martensite (SIM), and upon removal of the stress, the martensite being no longer stable, reverts back to the parent phase. However, there is one particular temperature, denoted M_D, above which martensite transformation cannot be induced by any amount of stress. In some cases, for example in NiTi, large strains of up to 8 % are associated with the stress-induced transformation. The driving force here is mechanical and not thermal.

3.2   Deformation Behavior of Martensitic and Austenitic NiTi

Martensitic or shape memory NiTi basically refers to NiTi that exists in the martensitic phase at room temperature and transformation temperatures for such an alloy varies with composition. A typical stress strain curve for such an alloy is shown in figure 3-3 (left). The initial elastic portion AB represents the elastic deformation of the untwinned martensite existing in the form of different randomly oriented variants, 24 in number[26]. When the stress level reaches a critical limit, the martensite starts twinning wherein the variants start coalescing and reorientation leading to the growth of one or more favored variants (BC). Subsequently, when the twinning process is complete, the elastic deformation of the twinned martensite is initiated and at D the twinned martensite deforms plastically and the associated plastic strain is not recoverable.

In the case of a superelastic NiTi that exists in the austenitic phase at room temperatures a typical stress strain curve would look like the one shown in figure 3-3 (right). Here the deformation

starts with the elastic deformation of the initial parent austenite phase and when the stress level reaches a critical limit A, the austenite transforms to martensite under the effect of the applied stress. The plateau represents the transformation and once the transformation is complete the SIM undergoes elastic deformation (BC). Upon unloading the SIM becomes unstable and reverts back to the austenite phase, below a critical stress level. It may be noted that as the temperature at which the stress is applied increases, above the M_s temperature, the critical stress that needs to be applied at that temperature for SIM formation also increases[26].

3.3 <u>Applications of Shape Memory Alloys</u>

The unique properties of SMAs have generated substantial commercial and scientific interest and have consequently led to their application for varied uses in different fields. New products are coming into the market each year. Some of the earliest applications included a temperature switch employing CdAgAu[27]. For some time NASA investigated the use of a SMA satellite antenna for the moon mission. However initially in the sixties the announced applications were mere collection of ideas. The large-scale fabrication of devices using SMAs began only in the seventies.

Some of the more prominent applications of SMAs can be classified as follows:

Industrial applications

Medical applications

Consumer applications

Examples of the above mentioned applications are numerous and their in-depth discussion is beyond the scope of this thesis. Only selected examples are presented here to highlight the

different ways in which the properties of SMAs can be used. More details can be found elsewhere [27-29].

3.3.1 Industrial Applications

Some of the more prominent industrial applications include connector, fastener and actuator applications.

Pipe couplings: This is one of the first areas where SMAs (TiNiFe ternary alloy)[29] were used. The transformation temperature of these alloys is well below the room temperature (-150°C). These alloys are used to form tubings with an inner diameter smaller than the outer diameter of the pipes they are intended to join, at room temperature. These tubings are then expanded after cooling them to below the M_f temperature and are maintained at that temperature until the pipes are inserted. Once this is done, the coupling is heated back to room temperature where they return to their original diameter firmly gripping the pipes. (See figure 3-4a) Thousands of such couplings have been used in the hydraulic systems of F-14 fighter jets.

Fasteners: When the far sides of the fastened objects cannot be accessed, as in enclosed mid-air structures, fasteners made from SMAs can be employed to solve the problem. Essentially, a fastener with a spread out end is formed at room temperature (austenitic phase) and then is taken below the transformation temperature where the ends are straightened out and then the fastener is inserted into the hole where upon reaching the room temperature the ends spread out to fasten the objects. (See figure 3-4b)

Actuators: These are one of the more widely used applications of SMAs. The primary advantage in using SMAs for actuators is the resulting small size of the component and also any additional moving parts are not required. Due to the absence of moving parts, lubricants and consequently sealings become redundant. The actuator also doubles as a sensor and generates higher forces and longer strokes when compared to conventional actuators.

3.3.2 Medical Applications

SMAs have rendered themselves favorably for use in the medical field primarily because of improved mechanical, chemical and biological properties, which includes capability for resistance against vivo degradation, decomposition, corrosion etc. Some of the more prominent medical applications include orthopedics (alloy implantation in the body for long periods), dentistry and components in medical devices and instruments.

One of the first bio-medical applications that achieved broad acceptance is the superelastic SMA for dental arch wires. These wires are attached to the teeth by small adhesively bonded clips and they provide the correcting force for adjusting the position of teeth. The resistance of these SMA wires to permanent deformation and their ability to apply a constant stress enables faster correction of the misalignment and far fewer periodic adjustments by the orthodontist.

Shape-memory bone fasteners are proving superior to the usual screwed metal plates when it comes to joining broken bones. The SMA plate is pre-strained and then attached to the two bone elements and as it warms to body temperature it pulls the mating surfaces into contact and thus accelerating the healing process.

In recent times, shape-memory stents are beginning to find widespread application in the human body. Stents are spiral tubular spring-like devices that are used to restore the potency of a vessel, which could be an artery, a duct or even the esophagus. Use of conventional polymers and metals for this application has proven to be only partially successful. The success of the SMA stent partially stems from the fact that these stents can be easily made in coiled form and then stretched to an almost straight rod shape to allow its placement in a catheter and then introduced at the desired location. On deployment the ribbon reforms into a rigid coil that supports the vessel walls. Other applications include the use of SMAs to improve spinal fusion or as long thin wires for placing catheters at the desired location in the body etc.

3.3.3   Consumer Applications

In addition to the aforementioned industrial and medical applications, SMAs find wide usage in more consumer products like eye glass frames, combination type air conditioners, electric ovens, coffee-makers, automatic dry boxes, pen recorders, cooling system for automobiles, temperature switches and temperature fuses and toys - that make use of the shape memory effect or their superelasticity.

Combination type air conditioners regulate temperatures year round pumping in hot air during the winters and cold air during the summers. Thus far, this was achieved by a combination of thermostats and motors that regulate the louver to either pump the hot air upward or the cold air downwards. SMA component replaces the combination of thermostats and motors by doubling as a sensor and actuator. Eyeglass frames make use of the superelastic nature of SMAs, rendering them more resistant to accidental damage as well as making them more attractive and

lightweight. SMAs have also been used as effective force generating devices. In one version developed in Japan [29] compressed NiTi cylinders are placed in a hole and then heated electrically whereupon the cylinders expand and fracture the cement or stone structure in which they are placed. Thus they not only reduce the noise and hazard associated with conventional explosives but can also be re-used. Superelastic SMA wires have also been used as cellular telephone antenna, making them more resistant to kinking and dents, and as stiffening wires in brassieres.

3.4   **<u>Figures</u>**
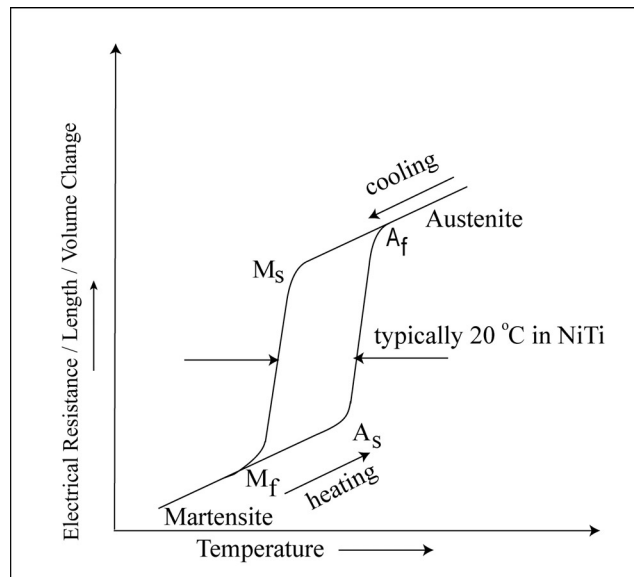
Figure 3-1: Hysteresis associated with martensite to austenite transformation.
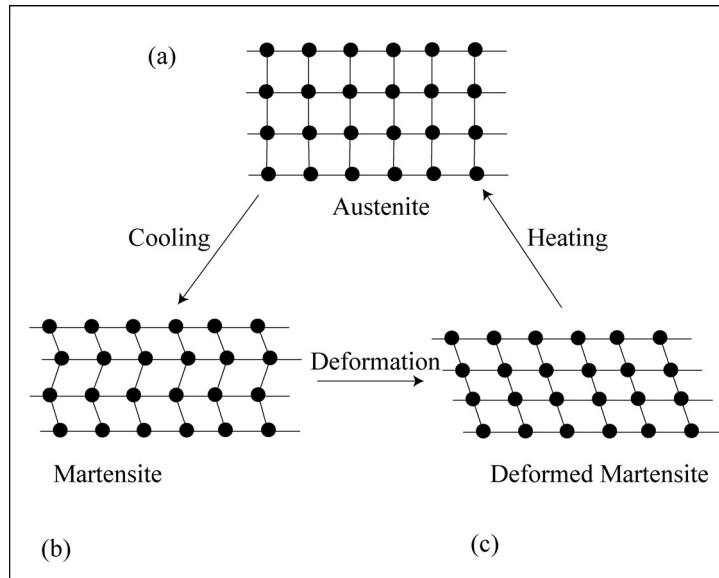
Figure 3-2: The shape memory effect, an atomic perspective[26].
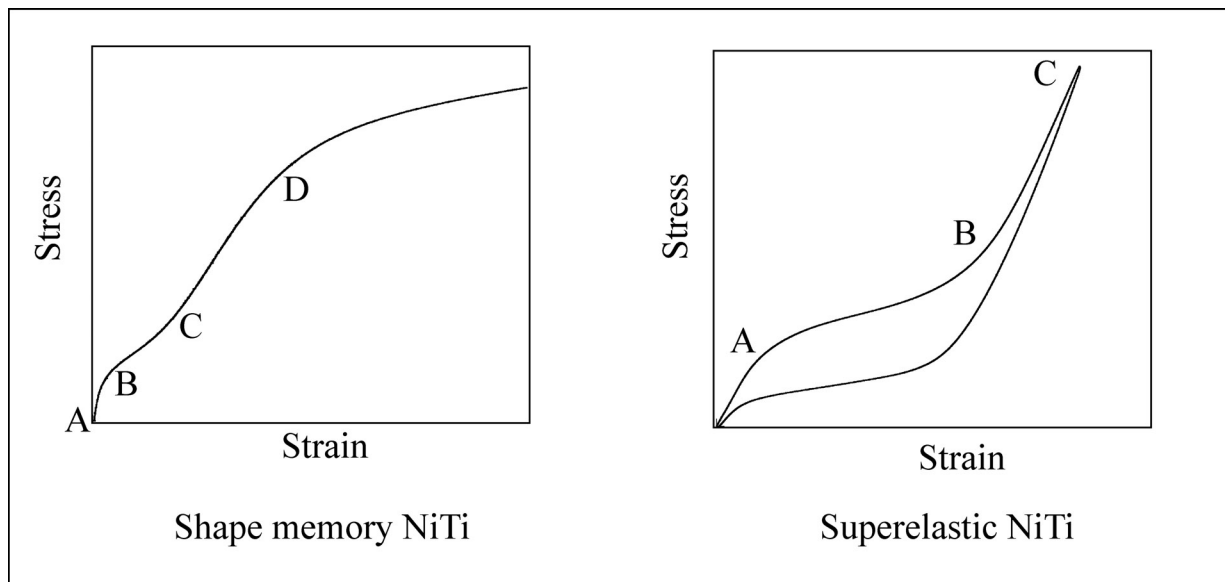
Figure 3-3: Typical stress vs. strain curve of shape memory and superelastic NiTi.

Pipes inserted after
expanding couplings

Heating

(a) SMA Coupling

(b) SMA Fasteners
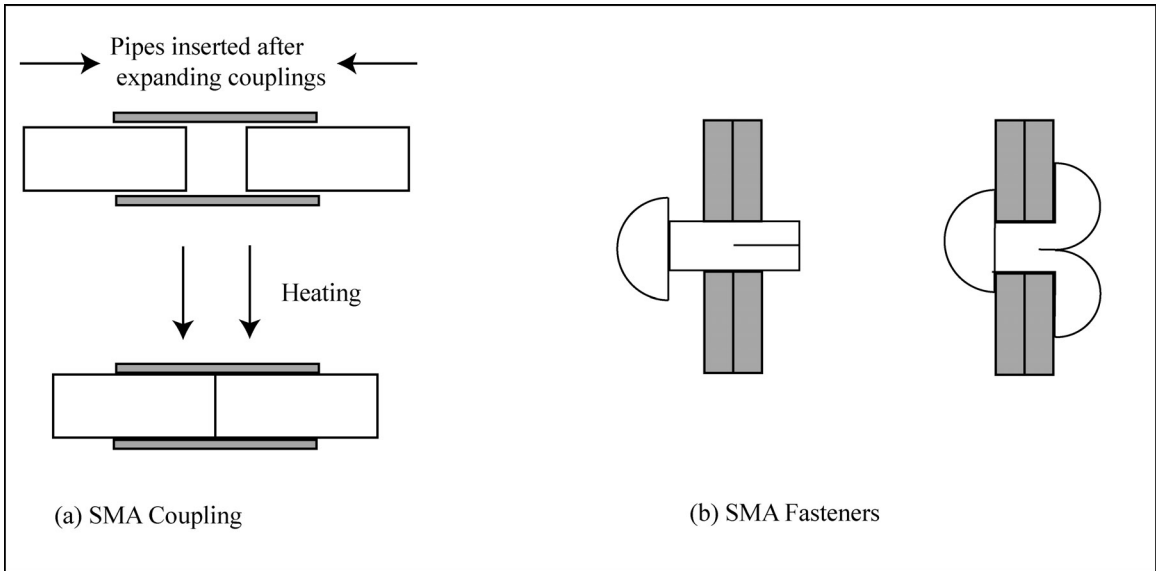
Figure 3-4: Applications of shape memory alloys.

4. STUDY OF DEFORMATION BEHAVIOR OF SHAPE MEMORY NiTi USING INSTRUMENTED INDENTATION – I

The deformation behavior of a shape memory NiTi studied using spherical indentation is presented in two parts. In this first part, the focus is on the elastic behavior of the material. The elastic modulus of B19' shape-memory NiTi was determined using three techniques; from the response of lattice planes measured using *in situ* neutron diffraction during loading, instrumented nanoindentation using a spherical indenter and macroscopic extensometry. The results thereof are presented here.

4.1 Objective and Brief Introduction to Neutron Diffraction

The stress-strain deformation response of martensitic NiTi may include contributions from elastic, twinning and plastic deformation, as discussed previously. In a macroscopic measurement using a strain gauge or an extensometer, it is impossible to distinguish between the different contributions. In particular, the relative contributions of twinning and plasticity are indistinguishable. It is not unreasonable to expect that deformation at low stresses, largely expected to be elastic, includes twinning strains that result in an artificially low elastic modulus. By recourse to *in situ* neutron diffraction during loading, instrumented nanoindentation and extensometry, the work presented in this chapter addresses these distinctions and obtains a modulus that is solely representative of elastic deformation.

The technique of using diffraction spectra for mechanical characterization relies on using atomic planes in specimens as internal strain gauges[30]. The distances between atomic planes, directly obtained from positions of peaks in diffraction spectra, can be used to compute strains. In

addition, the intensities of peaks in diffraction spectra can be used to ascertain texture or preferred orientation and phase volume fraction changes. For the case of shape-memory alloys, performing such diffraction measurements *in situ*, i.e., by simultaneously recording diffraction spectra from samples that are subjected to external stresses or temperature changes, can provide quantitative, phase specific information on the evolution of strains, texture and phase volume fractions[31-33]. The use of neutrons over x-rays from conventional sources is particularly advantageous in that they have added penetrability. This results in measurements being representative of the bulk in cm-scaled samples and not influenced by surface effects.

4.2 <u>Experimental Methods, Results and Discussion</u>

The NiTi samples investigated in this work were fabricated using hot isostatic processing (HIP) with a nominal composition of 49.4 atomic % Ni, as previously described[34]. Since starting texture is known to influence the deformation behavior of shape-memory alloys, HIP was used to produce samples with a random distribution of grains. The lack of texture in NiTi samples fabricated using HIP has previously been confirmed[34]. Prior to testing, samples were subjected to a solutionizing treatment at 930 ºC for 1 hour under titanium gettered flowing argon and furnace cooled to room temperature.

Neutron diffraction measurements were performed in "time-of-flight" mode using the neutron powder diffractometer (NPD) at the pulsed neutron source at Los Alamos Neutron Science Center (LANSCE), Los Alamos National Laboratory (LANL). Samples were loaded in uniaxial compression and tension while neutron diffraction spectra were simultaneously collected. The cylindrical compression sample had a diameter of 10 mm and a gauge length of 12.5 mm while

the tension sample had a rectangular cross-section of 7 X 4 mm and a gauge length of 25 mm. As shown in figure 4-1, the load axis was placed horizontally at 45° to the incident neutron beam (5 X 10 mm pulsed / standard collimation) and a detector (at -90°) recorded diffraction spectra with scattering vectors parallel to the loading axis. A second detector at +90 ° was also used but that spectra is included in a subsequent analysis[35]. Neutron diffraction spectra were obtained at six compressive stresses (5, 33, 66, 100, 200 and 300 MPa) and nine tensile stresses (5, 33, 75, 125, 150, 180, 200, 220 and 240 MPa) during loading. At each stress, a spectrum was acquired for about six hours at an average neutron beam current of 55 μA. The ramp rate was 0.1 mm/min. An extensometer was attached to the samples to record macroscopic strain during the experiments. The macroscopic stress-strain response determined from the extensometer during compressive and tensile loading is shown in figure 4-2. For completeness, in addition to the initial elastic response, figure 4-2 includes regions where twinning is the dominant deformation mechanism that is analyzed in a subsequent publication[35]. A fit to the initial linear portion (up to 40 MPa) of the tension and compression stress-strain response in figure 4-2 resulted in a Young's modulus of 68 ± 5 GPa (estimated error).

From the acquired neutron diffraction spectra, strains for specific grain orientations were determined by fitting individual lattice peaks with respect to the unloaded state using the RAWPLOT program in the General Structure Analysis System Software (GSAS)[36]. A nominal holding stress of 5 MPa was used as the "zero stress" unloaded condition. The strain, ε_{hkl}, for a plane, hkl, at a given stress was calculated from:

$$\varepsilon_{hkl} = \frac{d^{hkl} - d_0^{hkl}}{d_0^{hkl}}$$

4-1

where d^{hkl} was the spacing of the plane at a given stress and d_0^{hkl} was the corresponding lattice spacing in the unloaded or "zero stress" condition. Since the strains are relative, the presence of pre-existing residual intergranular stresses was ignored. Figure 4-3 shows the stress-strain response of selected individual lattice plane reflections. From this figure, the elastic moduli during compressive and tensile loading were determined to be (values for tension in parentheses) 122 (113), 91 (92) and 108 (130) GPa for the 011, 100 and 111 planes, respectively. The estimated error in the elastic moduli values is ± 5 GPa.

Instrumented nanoindentation provides a record of the indentation load (P) as a function of the penetration depth (h) of a tip (usually a diamond) into a specimen at nano-length scales, as described in detail earlier. Previous work has used indentation to qualitatively investigate shape-memory alloys[37-40]. The Nanotest 600 (Micromaterials Limited, Wrexham, UK) instrument, installed and commissioned as part of the author's masters thesis, was used to indent the aforementioned NiTi specimen. A custom spherical diamond indenter (2.8 mm diameter – see figure 5-2) was used and load-depth curves were obtained at a rate of 150 mN/s. The choice of this diameter was motivated by the need to indent about 10 grains for the depths reported. The machine compliance was determined by elastically indenting a standard steel specimen of know modulus. As an added check, the machine compliance determined using steel was used to determine the modulus of a fused quartz standard and values within 2 GPa of the standard were obtained. This calibration procedure is explained in further detail in the next chapter. Each indentation experiment on the NiTi sample consisted of indenting the specimen to a load of 0.5

N and unloading. The absence of substantial residual depth on unloading was suggestive of the nanoindentation response corresponding to mostly elastic deformation. As shown in figure 4-4, subsequent indents were performed at the same location as the 0.5 N indent, to loads of 2, 2.5, 3, 3.5, 4, 4.5 and 5 N, with complete unloading between indents at each depth. The purpose of adopting such a procedure was to progressively twin NiTi following the first predominantly elastic indent so that subsequent indents at the same location captured the response of the twinned martensite.

For elastic loading of a flat surface using a spherical indenter, the relationship between the load (P) and depth (h), as mentioned previously, is given by[11]:

$$P = Ch^{3/2},$$
2-5

where

$$C = \frac{2\sqrt{2}}{3} E^* D^{1/2},$$
2-6

D is the indenter diameter and

$$E^* = \left(\frac{1 - v_1^2}{E_1} + \frac{1 - v_2^2}{E_2} \right)^{-1}.$$
2-2

E^* is a reduced elastic modulus that accounts for non-rigid indenters, where E_1 and v_1 represent the elastic modulus and the Poisson's ratio of the indenter, respectively, and E_2 and v_2 represent the elastic modulus and the Poisson's ratio of the material being indented, respectively. The elastic portion of the first (0.5 N) and last (5 N) indents were fit to a 3/2 power law to determine C in equation 4-3 as shown in figure 4-5 . Using a value of 1141 GPa for diamond, 0.07 and 0.35 (ref. [41]) for the Poisson's ratios of diamond and NiTi, respectively, the elastic modulus of NiTi

was determined to be 101 ± 7 GPa and 162 ± 6 GPa for the first (0.5 N) and last indents (5 N), respectively. The errors reported represent a standard deviation from 15 comparable indents.

The Young's modulus of martensitic NiTi determined from extensometry in this work (68 ± 5 GPa) is comparable with values previously reported and justified (69 ± 4 GPa)[41]. Even values as low as 20-50 GPa have been reported[42,43]. The extensometry values are substantially lower than the values obtained here from neutron diffraction and indentation. Given the low symmetry of monoclinic NiTi, it is not straightforward to account for elastic anisotropy and obtain an average Young's modulus from the neutron diffraction measurements. However, the moduli of the lattice planes reported can be expected to reflect the average bulk polycrystalline response as seen previously for the case of cubic (B2) NiTi[32]. This is consistent with the modulus determined from indentation (101 GPa) lying in the range of lattice plane moduli determined from neutron diffraction (91-130 GPa). In the context of the aforementioned lower modulus from extensometry, figure 4-6 is presented to establish twinning at low stresses, in what is nominally an elastic regime for the macroscopic measurement. Figure 4-6 shows the 011 peak intensities with increasing compressive stress from neutron diffraction spectra that have been normalized so that spectra at each stress have the same total intensity (neutron counts). $(11\bar{1})$Type I twinning in martensitic NiTi has been shown to result in 011 planes lying parallel to the loading axis under compressive loading[41]. From the scattering geometry in figure 4-1, this would result in the 011 peaks decreasing in intensity, for the detector considered. This is indeed the case in figure 4-6, confirming that at very low stresses (33 and 66 MPa) martensitic NiTi undergoes twinning that results in additional strains, that in turn result in a lower Young's modulus from extensometry. While the technique of neutron diffraction inherently measures elastic strain (as opposed to non-

34

elastic strains which can only be measured when they influence elastic strains) and is not expected to be significantly influenced by the limited twinning at low stresses, it is interesting to examine why instrumented indentation is not influenced by twinning as is extensometry. For this, consider that the in-plane shear stress under a spherical indenter is maximal at a ratio of depth to indenter contact half-width of 0.48 (figure 4-7), and not directly below the indenter[44]. The surrounding material at this depth may spatially constrain twinning at low stresses. Twinning eventually does occur, but at higher stresses.

4.3   Conclusion

The present work suggests stress-strain curves of martensitic NiTi using macroscopic extensometry includes strain from twinning that results in a low Young's modulus, that are not truly representative of elastic deformation. Twinning at stresses as low as 33 MPa has been experimentally observed using neutron diffraction. On the other hand, determination of the elastic modulus using instrumented spherical nanoindentation and lattice plane moduli from *in situ* neutron diffraction during loading result in values that are about 50 % higher and are not influenced by twinning.

4.4 **Figures**
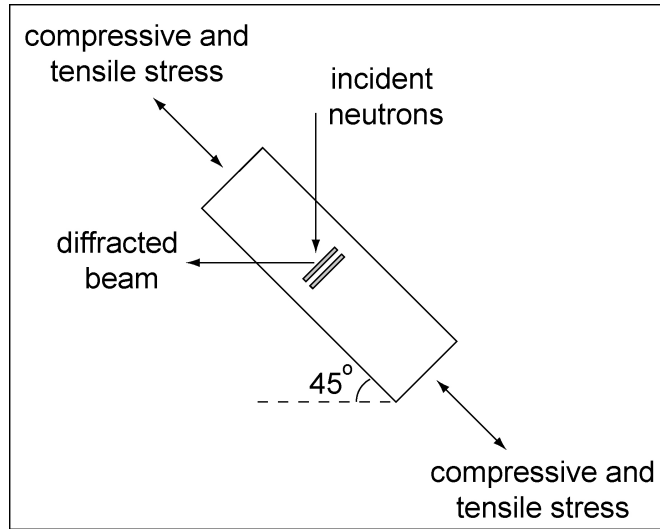
Figure 4-1: Schematic of the experimental setup at Los Alamos National Laboratory showing the incident neutron beam and the diffracted beam. The irradiated volume is about 1 cm^3.
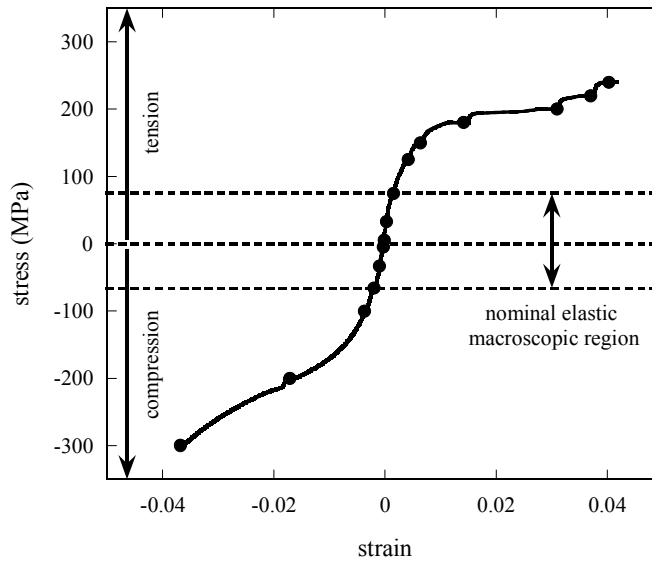
Figure 4-2: Applied stress vs. macroscopic strain measured by extensometry for NiTi in tension and compression. The symbols indicate the stresses at which neutron diffraction spectra were obtained during loading.
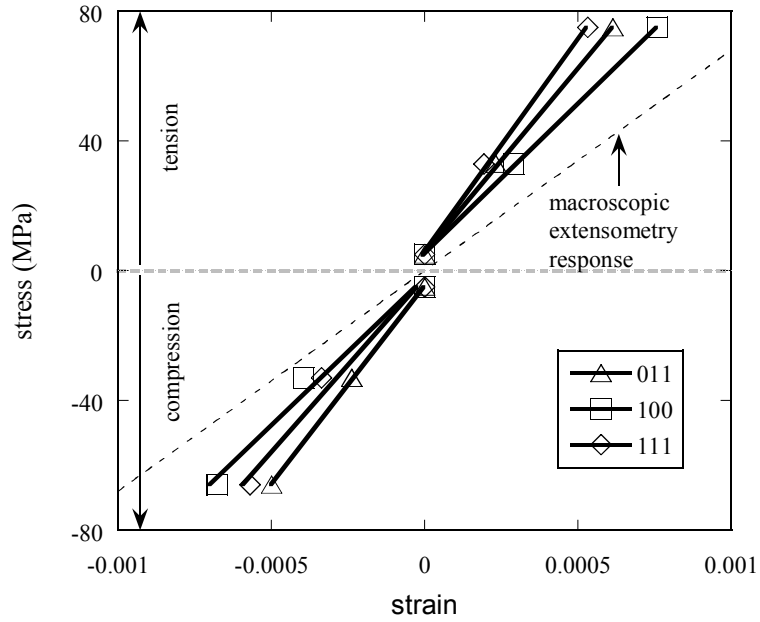
Figure 4-3: The stress-strain response of individual lattice plane reflections in NiTi during loading in tension and compression.
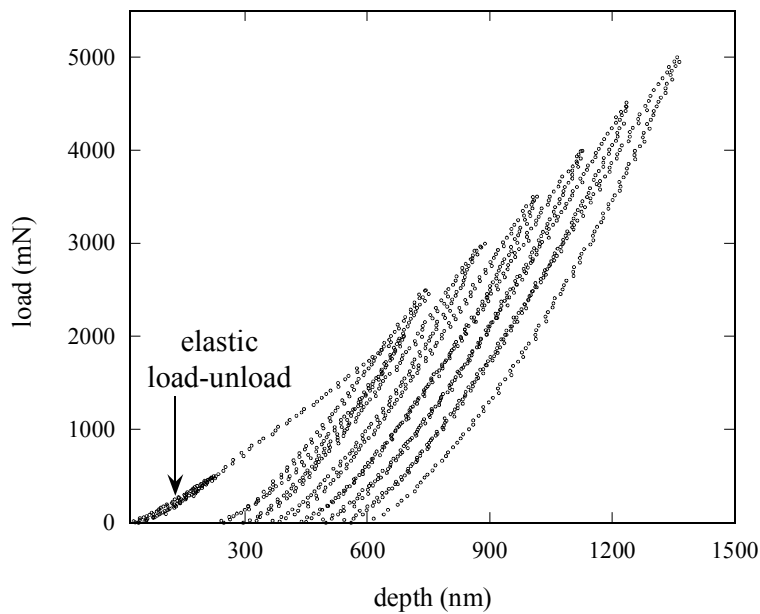
Figure 4-4: Nanoindentation response of NiTi using a spherical diamond indenter. Load-unload experiments at the same location were performed to progressively higher loads. The initial elastic response corresponding to a load-unload experiment to 0.5 N is marked.
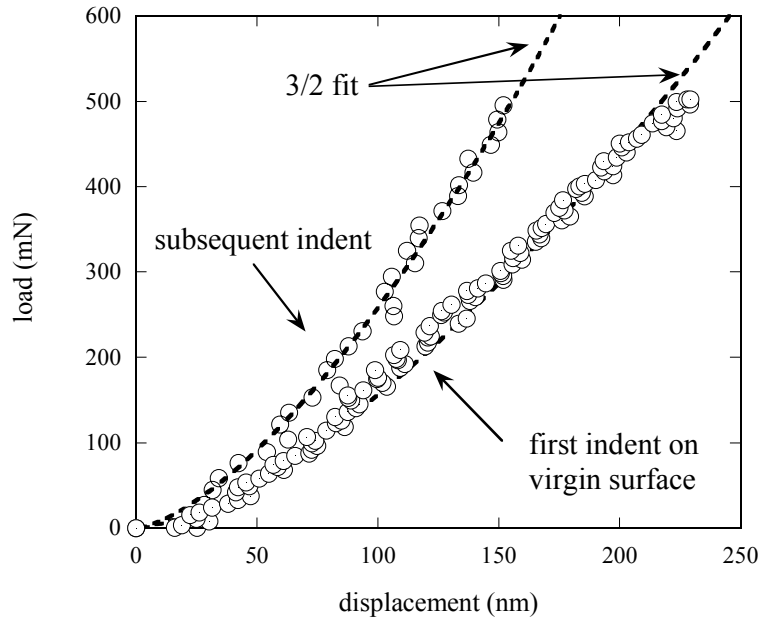
Figure 4-5: A 3/2 power fit to the elastic portion of the P-h response corresponding to the first indent on a virgin surface and a subsequent indent to determine the elastic modulus of the B-19' martensite before and after twinning, respectively.
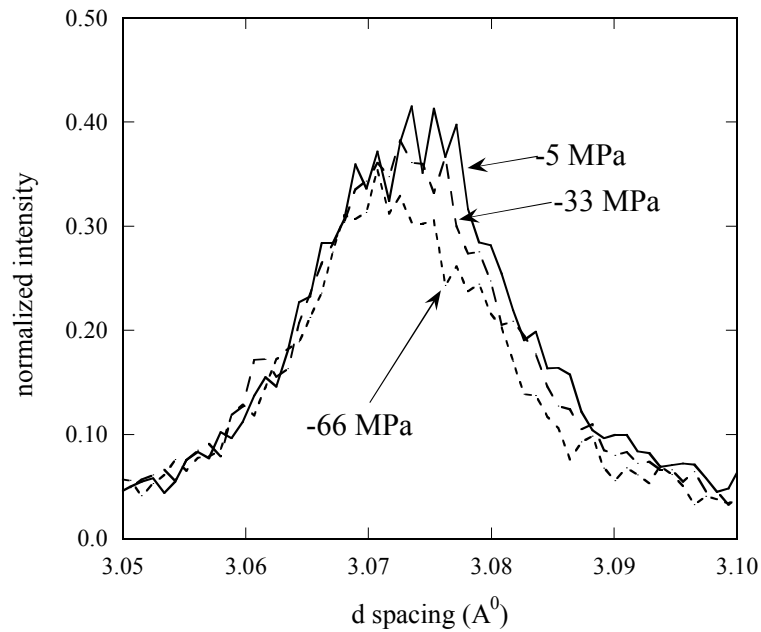
Figure 4-6: Section of normalized neutron diffraction spectra from NiTi at -5, -33 and -66 MPa (compressive loading) corresponding to 011 lattice plane reflections.
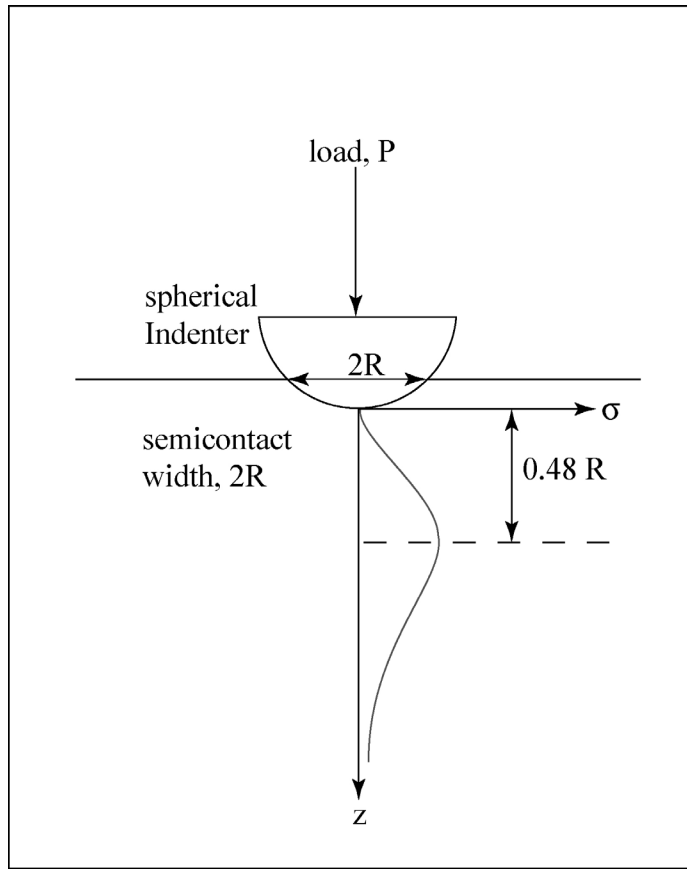
Figure 4-7: Maximum shear stress under an spherical indenter.

5. STUDY OF DEFORMATION BEHAVIOR OF SHAPE MEMORY NITI USING INSTRUMENTED INDENTATION - II

The deformation behavior of the B19' martensite was studied beyond the initial elastic deformation. Custom designed diamond spherical indenters have been used to effectively capture events such as twinning and elastic deformation following twinning. The indentation response of the NiTi shape memory alloy has been partially correlated to its macroscopic stress strain behavior. The spherical indentation response of a shape memory NiTi has been contrasted with its mechanical behavior under a sharp Berkovich indenter and finally finite element modeling has been used to validate experimental results. Calibration procedures to account for the machine compliance is also detailed.

5.1 Background

The efficacy and advantages of instrumented indentation in measuring the mechanical properties of materials was discussed earlier. It was also mentioned that methodologies for extracting a variety of mechanical properties from the nanoindentation P-h curves have been established. However a majority of these methodologies focus on property extraction using a sharp indenter such as a Berkovich indenter. Moreover most of these techniques are applicable to materials whose mechanical behavior is typified by a largely straightforward elasto-plastic stress strain response. While materials where alternate mechanisms for deformation are available, specifically SMAs, have been probed using instrumented indentation before[37-40,45], a comprehensive methodology for property extraction using instrumented indentation for these materials is lacking.

NiTi SMAs are a class of materials whose mechanical behavior and thereby the functionality, is influenced to a large extent by a phase transformation between a low symmetry martensitic phase (B19') and a high symmetry austenitic phase (B2). While this was discussed in detail previously, it is briefly summarized here. In the case of the Ti rich alloys, this transformation is driven thermally (at room temperatures) and is known as the shape memory effect. When the alloy is Ni rich the transformation is stress driven (at room temperatures) and gives rise to superelasticity. In both cases strains of up to 8 % can be accommodated. While in the latter case this strain recovery is spontaneous upon unloading, in the former heating is required after unloading. These alloys have found extensive use in the biomedical industry as materials for vascular stents, orthodontic arch wires, rotary dental drills and cardiovascular guide wires whose very functionality depend on the mechanical behavior of these alloys. The performance of these and other emerging biomedical devices such as microdevices, orthopedic fixation mechanisms etc. can be optimized by precisely controlling the chemical composition and thereby the transformation temperatures and the mechanical behavior. Given the sensitivity of the transformation temperatures of these alloys to their chemical composition[46], optimizing themomechanical processing parameters prior to large scale production becomes imperative and nanoindentation is a relatively cost effective means of doing this because of its inherent ability to extract mechanical properties from relatively small sampling volumes e.g., intricate SMA geometries (strips or wires) or medical devices such as stents etc.

The macroscopic stress-strain response of a shape memory NiTi was described previously and is reproduced here for ease of reading. Typically this shows three distinct regions as illustrated in figure 5-1. The initial part AB is generally believed to be pure elastic deformation of the B19'

martensite. BC represents twinning induced inelastic deformation and once twinning is exhausted, the twinned martensite is believed to undergo pure elastic deformation, represented by CD in figure 5-1, followed by plastic deformation beyond D.

In the work presented here, the indentation behavior of a shape memory NiTi (Ti rich) has been studied with the following objectives in mind:

a) determine the onset of twinning after the initial elastic deformation of the B19' martensite from the nanoindentation response;

b) to study the deformation behavior of the B19' martensite beyond twinning and determine its Young's modulus and the onset of large scale plastic deformation following twinning; and

c) co-relate the above microscopic indentation response of the shape memory NiTi, atleast in part, to its macroscopic stress-strain response.

5.2   Materials and Methods

The shape memory NiTi sample (nominal composition of 49.4 atomic percent Ni) investigated in this work was fabricated using hot isostatic pressing (HIP), to avoid the influence of starting texture on the deformation behavior of the sample. The lack of texture in the sample fabricated using HIP was previously confirmed[34]. Prior to testing, the samples were subjected to a solutionizing treatment at 930 $^{\circ}$C for 1 hour under titanium gettered flowing argon and furnace cooled to room temperature.

A Nanotest 600 (Micromaterials Limited, Wrexham UK) was used to indent the above sample. A custom 2.8 mm diameter diamond spherical indenter, figure 5-2, was used for the indentation experiments and all indentation experiments were performed at room temperature. A spherical indenter was preferred over a sharp indenter in order to obtain a non-singular stress field under the indenter and delay the onset of twinning and plastic deformation (in terms of indentation depth) during deformation and the choice of this diameter was partly motivated by the need to indent about 10 grains for the depths reported. To account for the instrument compliance, the total displacement, h_{total}, was modeled as follows:

$$h_{total} = h_{instrument} + h_{sample} \hspace{4cm} \text{5-1}$$

The instrument's load – displacement relation was then determined by elastically indenting a standard steel specimen of known Young's modulus (210 GPa). The load-displacement relation of the instrument, thus obtained, is as shown in figure 5-3, and a linear fit to the data gives an expression for $h_{instrument}$ as a function of the applied load. As an added check, the relationship obtained above was used to determine the modulus of a standard fused quartz specimen and values within 2 GPa of the standard were obtained as shown in figure 5-4. In the subsequent analyses of indentation results from NiTi SMA, the above methodology was used to correct the raw data for instrument compliance.

To capture the initial elastic response of the martensite before the onset of large scale twinning, the specimen was indented to a load of 0.5 N and the corresponding results and conclusions have been reported in the previous chapter. Subsequently, the specimen was indented at the same location to progressively higher loads in steps of 0.2 N with complete unloading between indents at each depth, up to a maximum of 19.5 N. A total of 96 indents were made at the same location.

The purpose of adopting such a procedure was to progressively twin NiTi following the first predominantly elastic indent so that subsequent indents at the same location captured the response of the twinned NiTi. A loading rate of 150 mN / s was used throughout. In addition to the formulation described in the previous chapter, to determine elastic properties by spherical indentation, the following expression[44] was used to estimate the maximum shear stress, τ_{max}, under the indenter at any given load.

$$\tau_{max} = 0.31 \left(\frac{6PE^{*2}}{\pi^3 R^2} \right)^{1/3}$$
5-2

where P is the load, E* is a reduced elastic modulus that accounts for non-rigid indenters and R is the radius of the indenter.

The NiTi specimen was also indented using a standard sharp Berkovich indenter. The virgin surface was indented up to a maximum load of 0.75 N and 3.5 N at a rate of 100 mN / s. Here, the elastic properties were determined using the analysis procedure proposed by Oliver & Pharr[9] from the unloading portion of the P-h response.

5.3 <u>Experimental Results</u>

5.3.1 Spherical Indentation

The first indents on a virgin surface were analyzed to estimate the elastic modulus of the B19' martensite before twinning, corresponding to region AB in figure 5-1. The corresponding results and comparisons with *in situ* neutron diffraction measurements and extensometry results were presented in the previous chapter. Following the initial elastic deformation, the martensite

undergoes twinning at some critical stress. The onset of large-scale twinning was captured by plotting log load (P) against log displacement (h) for the loading portion of the P-h response corresponding to a maximum load of 2 N, as shown in figure 5-5. Since the elastic loading of a flat surface using a spherical indenter yields a P-h curve that follows a 3/2 power law, as proposed by Hertz[12], the loading curve shows a deviation from the 3/2 slope with the onset of large scale inelastic twinning. The maximum shear stress under the indenter corresponding to the load at the point of deviation was found, using equation 5-2, to be 274 MPa in this case.

Subsequent indents at the same location, as shown in figure 5-6, were analyzed to extract the elastic properties of the twinned martensite. The residual depth corresponding to each of the subsequent indents was tracked as a function of the maximum load of the indent, as shown in figure 5-7. Three distinct regions are evident. Stage I where there is a progressive increase in the residual depth initially which then begins to plateau out at loads corresponding to about 7 N; Stage II where the residual depth starts to drop sharply and attains a minimum value (point A in figure 5-7); and Stage III where it begins to increase again. The increasing residual depth in Stage I can be attributed to twinning. A subsequent drop in residual depth (Stage II) is because of the predominantly elastic deformation of the twinned martensite. Pure elastic deformation of the twinned martensite is often suggested to be the main mode of deformation following twinning. However this is contrary to what is observed here. This is suggested by the gradual drop in residual depth rather than an abrupt drop to a near zero value. Consequently, twinning seems to co-exist with elastic deformation of martensite. Following the minimum at A, there is a linear increase in residual depth, which is indicative of large-scale plastic deformation. Apparently, Hertzian analysis of the P-h curve corresponding to A in figure 5-7 should yield an elastic

modulus for the twinned martensite. The elastic modulus value reported in the previous chapter was obtained by following such a procedure. However, indents made at the same location are not on a flat surface because of the cavity or indent impression (due to twinning) left behind by the previous indents. Consequently, the elastic modulus obtained using Hertzian analysis is overestimated for such a case[44,47]. In order to obtain an accurate value of elastic modulus for the twinned martensite finite element modeling (FEM) was employed. The profile of the indented surface after the 83rd indent (corresponding to point A in figure 5-7) was measured using the nanoindenter as a profilometer, as shown in figure 5-8, and the radius of curvature and the depth of the cavity were determined to be 1.3 mm, which approximately equals that of the diamond indenter, and 3.0 μm respectively. This profile was modeled as an axisymmetric isotropic linear elastic solid (10^6 nm X 10^6 nm) in SDRC I-DEAS finite element package. Axisymmetric quadrilateral elements were used with a finer mesh size around the cavity as shown in figure 5-9. The model was subsequently translated into ABAQUS[48] and indentation simulations using a rigid indenter were executed on ABAQUS. The Poisson's ratio used for the material was 0.35 (ref. [41]). The elastic modulus of the material was varied to match the P-h response generated by the FEM with the experimental P-h response corresponding to the 83rd indent at A in figure 5-7. The elastic modulus value thus obtained was 17.7 GPa for the twinned martensite as shown in figure 5-10. From conventional Hertzian theory a P-h curve corresponding to an E value of 17.7 GPa would be expected to lie to the right of or below the P-h curve corresponding to that of the higher 95 GPa. However this is true only for the case of a spherical indenter indenting a flat surface. Here repeated indentations at the same location render the surface "non-flat" and hence the indentations on the resulting cavity stiffen the P-h response substantially to push the P-h

curve corresponding to an E value of 17.7 GPa above and to the left of the P-h curve corresponding to that of the higher 95 GPa.

FE simulations of a rigid spherical indenter indenting a *flat* surface with similar dimensions and meshing as above were also performed and results compared with Hertzian analytical predictions, as shown in figure 5-10. The good agreement between the two established the accuracy of the model.

5.3.2 Sharp Indentation

Figure 5-11 presents the P-h response obtained by indenting the shape memory NiTi using a standard Berkovich indenter. For the elastic loading of a flat surface using a Berkovich indenter, the relationship between the load (P) and depth (h) is given by[7,49]

$$P = Ch^2 = 2.1891(1 - 0.21\nu_i - 0.01\nu_i^2 - 0.41\nu_i^3)E^*h^2 \qquad \text{2-1}$$

where E* is the reduced modulus described earlier and ν_i is the Poisson's ratio of the indented material. Hence to isolate the elastic deformation and estimate the elastic modulus using the above expression, log P was plotted against log h for the loading portion of the curve as presented in figure 5-12. However as is evident from the figure the data fits a line with a slope of 2 very poorly. This is attributed to the early onset of plastic deformation in the case of a sharp indenter because of the inherently higher magnitude of stresses under a sharp indenter. This relegates any elastic deformation to very small loads. To circumvent this problem, an "overall" elastic modulus value of 71 $\pm$ 4.3 GPa was estimated from the initial slope of the unloading portion of the curve, as proposed by Oliver & Pharr[9], for the material.

5.4   Discussion

The experimental results from spherical indentation are discussed here sequentially in correlation to the macroscopic stress strain behavior described earlier. The first indents on a virgin surface up to a load of 0.5 N yielded a purely elastic response and was reported and discussed in the previous chapter. It was also shown that the elastic modulus for martensite in this region (AB in figure 5-1) was 101 ± 7 GPa, which was substantially higher than values obtained using a conventional extensometer. This difference was attributed to twinning at very low stresses in a macroscopic tensile test which is otherwise delayed in spherical indentation because of the maximum stress under the indenter being some distance away from the surface and the surrounding material there constraining twinning.

Subsequently, in this work, the maximum stress under the indenter corresponding to the point B in figure 5-1 or onset of large scale twinning was estimated by plotting log load (P) against log displacement (h) for the loading portion of the P-h response corresponding to a maximum load of 2 N on a virgin surface, since twinning is an inelastic deformation mechanism. This onset of large-scale twinning can also be detected by plotting the residual depth against peak load, from indents at the same location to progressively higher loads, as shown in figure 5-7. However, this region occurs in the initial stages of loading and is not shown in figure 5-7. More importantly though, following such an approach, critical events such as onset of elastic deformation of martensite post- large scale twinning and subsequent plastic deformation have been identified from instrumented indentation data for the first time. While the increasing residual depth in Stage I can be attributed to twinning with progressively increasing loads, it is interesting to examine why the residual depth in Stage II does not drop off to zero instantaneously as would be

expected with the onset of pure elastic deformation. A rather gradual drop in residual depth to a minimum value close to zero is indicative of deformation in this region not being purely elastic but having inelastic strain contributions from twinning. Hence, the elastic modulus value of about 17 GPa reported here can be expected to be somewhat deflated. This is however greater than the modulus value of 11.7 GPa obtained by conventional extensometry for the same material. This increase can be explained by the fact that even though in Stage II we have substantial strain contributions from twinning, the maximum stress under the indenter is still some distance below the indenter where the surrounding material offers resistance to twinning. Figure 5-13 is presented to establish this where the stress contours computed using FEM clearly show a maximum at some distance below the indenter. While for the case of a spherical indenter deforming a *flat* surface, this was predicted by the Hertzian theory[44], this appears to be true even for the case of a spherical indenter indenting a cavity.

The results presented here can be broadly classified as providing valuable information at two levels. One, about the technique of instrumented nanoindentation and its applicability vis-à-vis SMA and secondly, a better understanding of the mechanical behavior of NiTi SMA; and both of these have important ramifications on the applicability of NiTi as an engineering material.

The presented indentation methodology initiates nanoindentation as a convenient cost effective technique of optimizing thermomechanical processing parameters especially given the need to control the stress strain behavior to optimize product performance. Alternatively, this technique can be used as a quality control tool where critical transformation stresses and thereby the transformation temperatures can be effectively monitored directly testing actual devices rather

than making standard test specimens. However the spherical indentation methodology described here is not limited to the case of NiTi but can be easily extended to other materials as well and can be an easy way of detecting the onset of large scale plasticity.

The present study has also provided important insight into the deformation behavior of the shape memory NiTi. For example, it has been conventionally believed that the macroscopic deformation behavior of NiTi, as shown in figure 5-1, can be clearly demarcated into several regions, which are either purely elastic or purely inelastic. However this does not seem to be so. Martensite twinning was observed at low stresses and reported in the previous chapter. This study shows that twinning does not end at point C in figure 5-1 but is an active deformation mechanism even when the twinned martensite is believed to be deforming elastically. These along with the modulus values reported here are of critical importance and can have important ramifications for various applications. For example, these can be valuable inputs for a constitutive model that can make accurate predictions. Such a model coupled with finite element analysis can render alloy development accurate, cost effective and fast.

5.5 Conclusion

The following conclusions can be drawn –
  i. twinning following the initial elastic deformation of the B19' martensite was successfully identified for the first time from a nanoindentation response and the corresponding maximum shear stress under the indenter was estimated to be about 274 MPa;

ii. the onset of predominantly elastic behavior of the B19' martensite following twinning was determined and the Young's modulus of the twinned martensite was determined to be about 17.7 GPa;

iii. an overall elastic modulus value of about 71 GPa for the material was obtained using a sharp Berkovich indenter;

iv. subsequently, based on the above results, the nanoindentation response of a shape memory NiTi was partially linked quantitatively to its macroscopic response; and

v. from a much broader perspective it was shown that the deformation behavior of NiTi SMAs is not a straightforward process with clearly demarcated regions of elastic and inelastic deformations. These regions overlap and co-exist which renders elastic modulus values measured using conventional extensometry deflated. The elastic modulus of the martensite before and after twinning using instrumented indentation is substantially higher than from extensometry. This can be attributed to the fact that the maximum stress under a spherical indenter is some distance below the surface where the surrounding material geometrically constrains twinning.

5.6   Figures
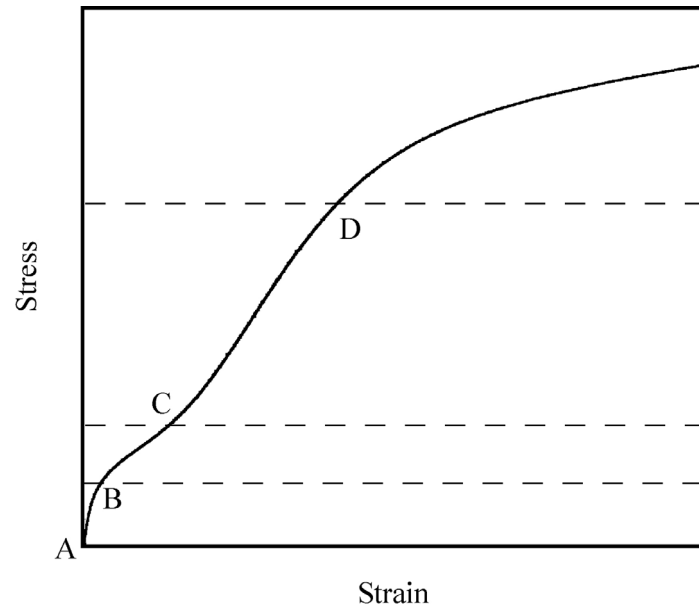
Figure 5-1: A typical macroscopic stress-strain response of a shape memory NiTi.
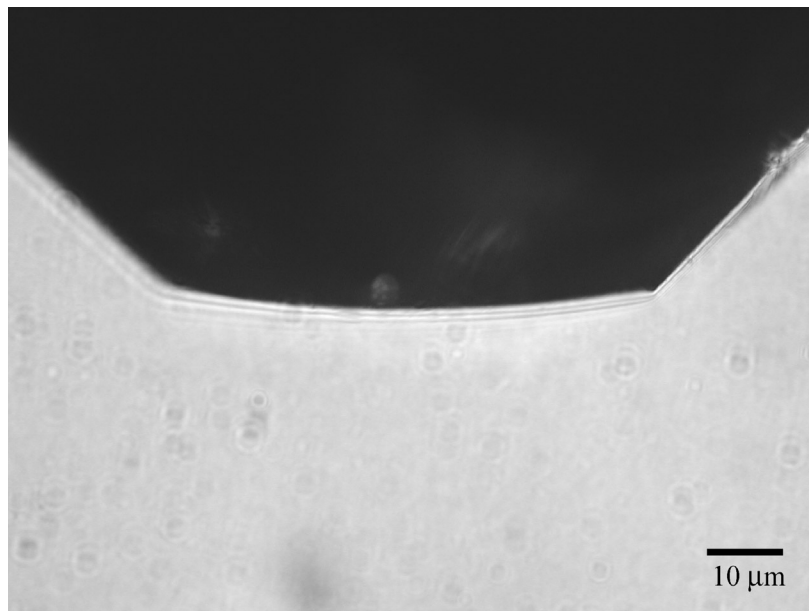
Figure 5-2: The 2.8 mm diamond spherical indenter used in the present work.
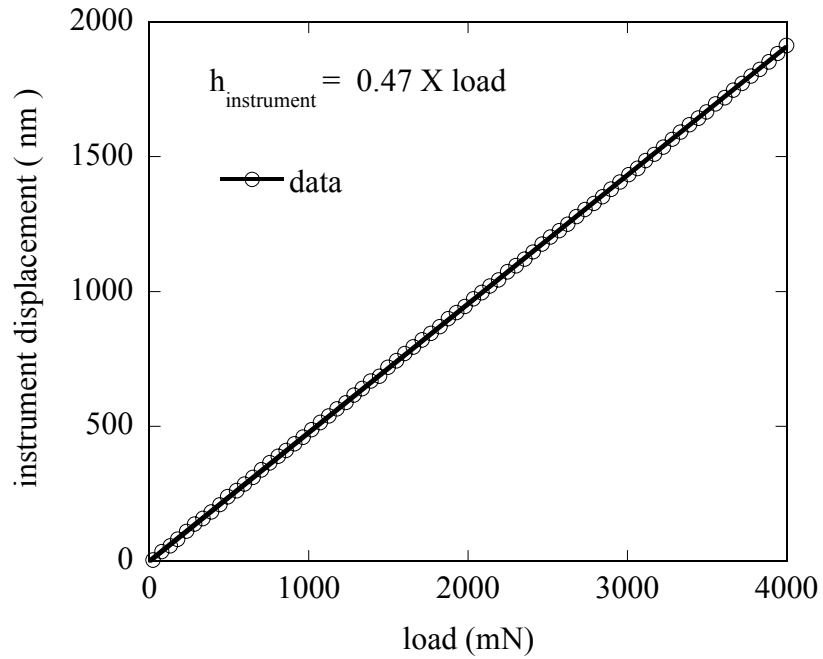
Figure 5-3: Machine Compliance. The linear relation between machine defomation and applied load.
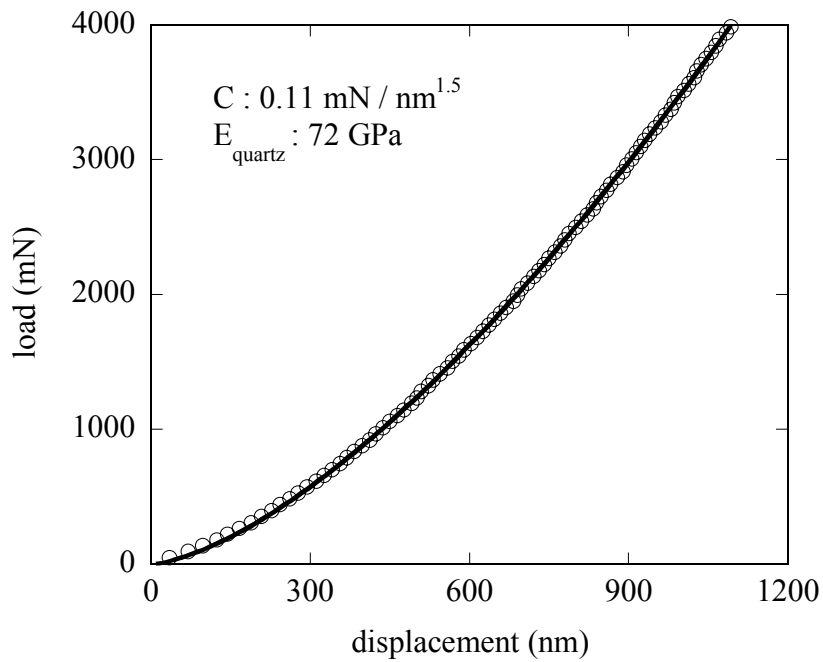
Figure 5-4: A 3/2 fit to the loading portion of the load-depth response of the standard fused quartz for compliance verification.
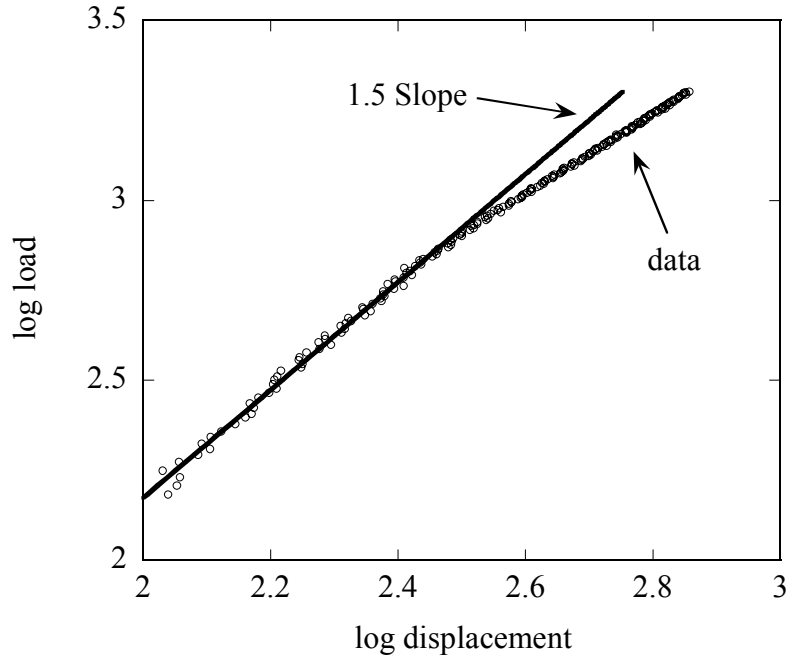
Figure 5-5: Log load (P) against log displacement (h) for the loading portion of the P-h response corresponding to a maximum load of 2 N on a virgin surface.
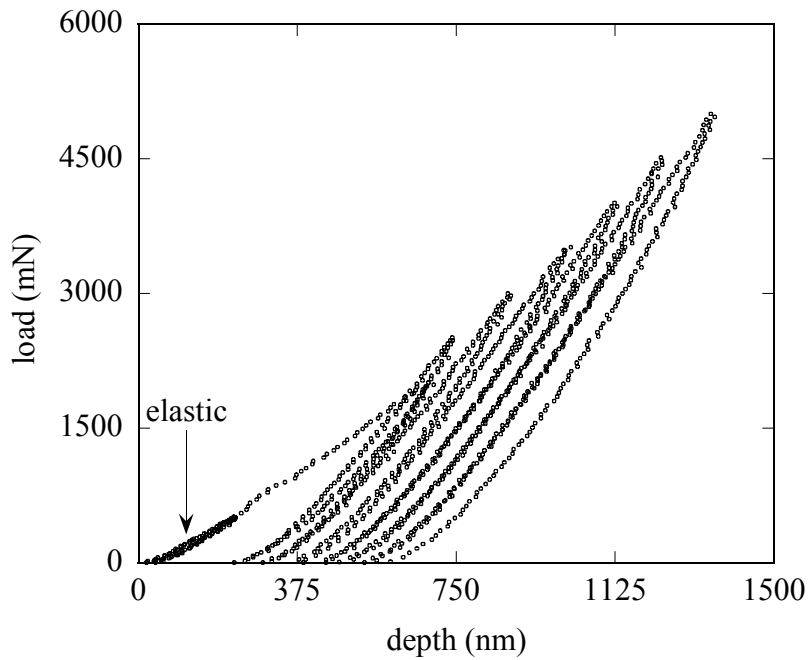
Figure 5-6: Load depth response resulting from indentations at the same location to progressively higher loads. Only the initial portion is shown here for the sake of clarity.
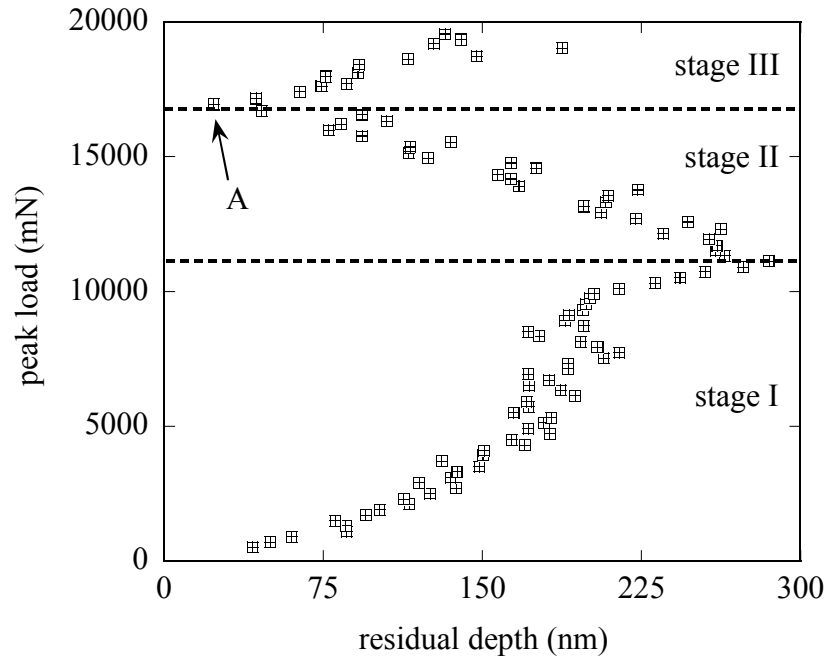
Figure 5-7: Residual depth from subsequent indents plotted as a function of peak load.
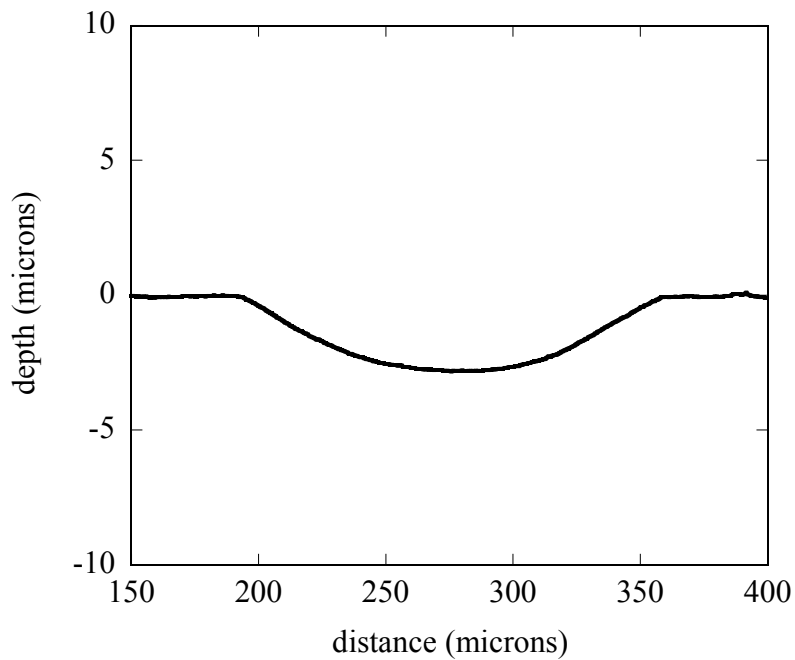
Figure 5-8: The actual profile of the indented surface after 83 indents at the same location to progressively higher loads, measured using the indenter as a profilometer.
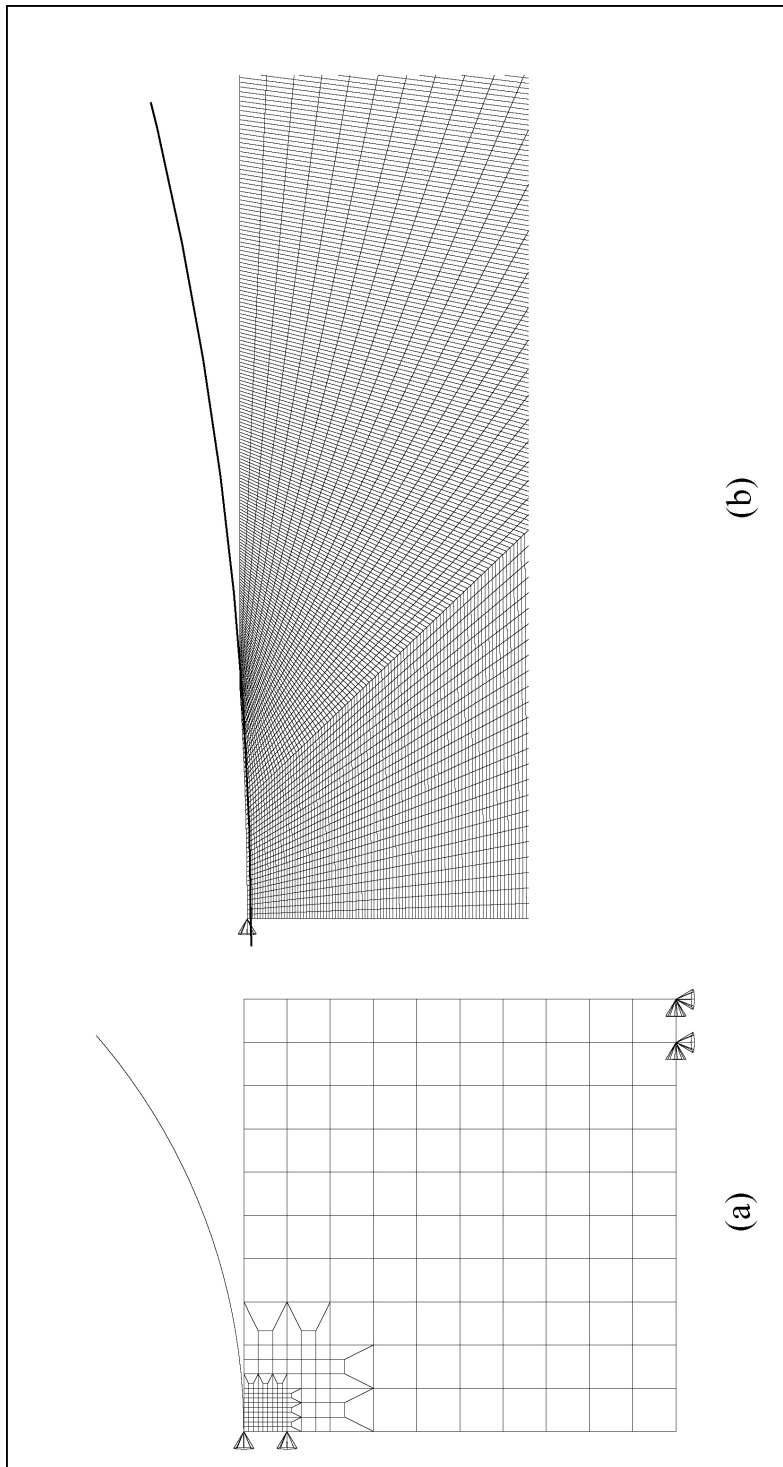
Figure 5-9: (a) FE model and associated meshing for indentation on a flat suface using a spherical indenter; (b) Close-up of the FE model and associated meshing for indentation of a 3 µm deep cavity on a surface with a spherical indenter.
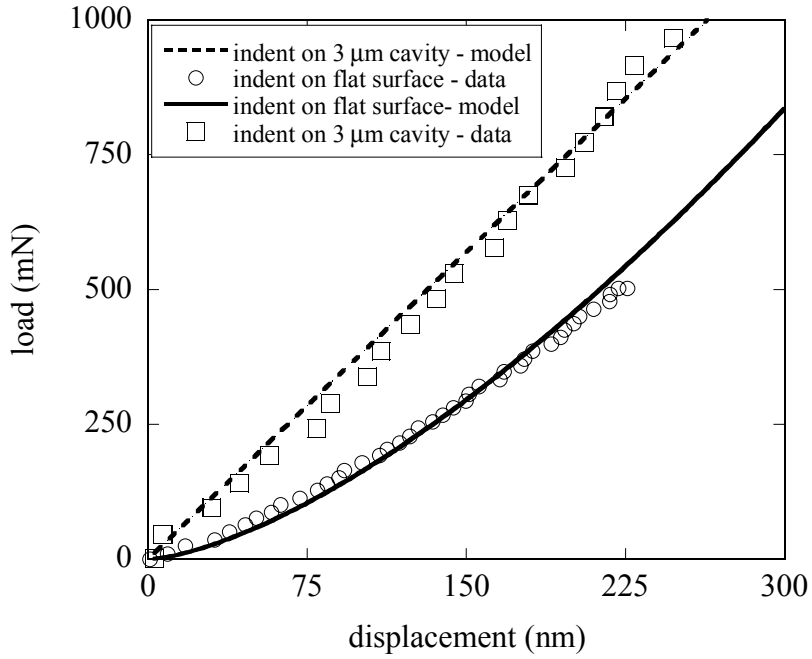
Figure 5-10: FE and experimental results compared.
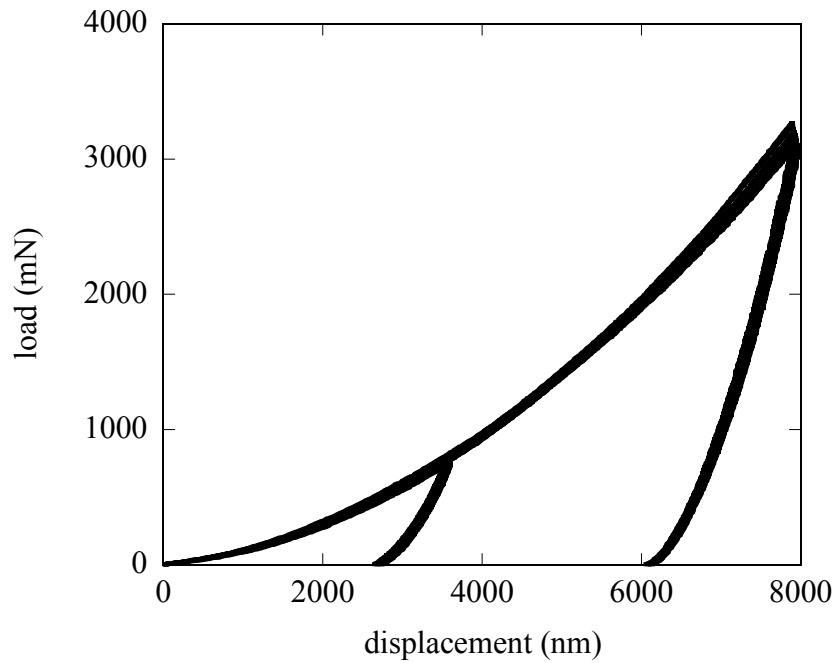
Figure 5-11: Load depth response, corresponding to two peak loads, of shape memory NiTi using a sharp Berkovich indenter.
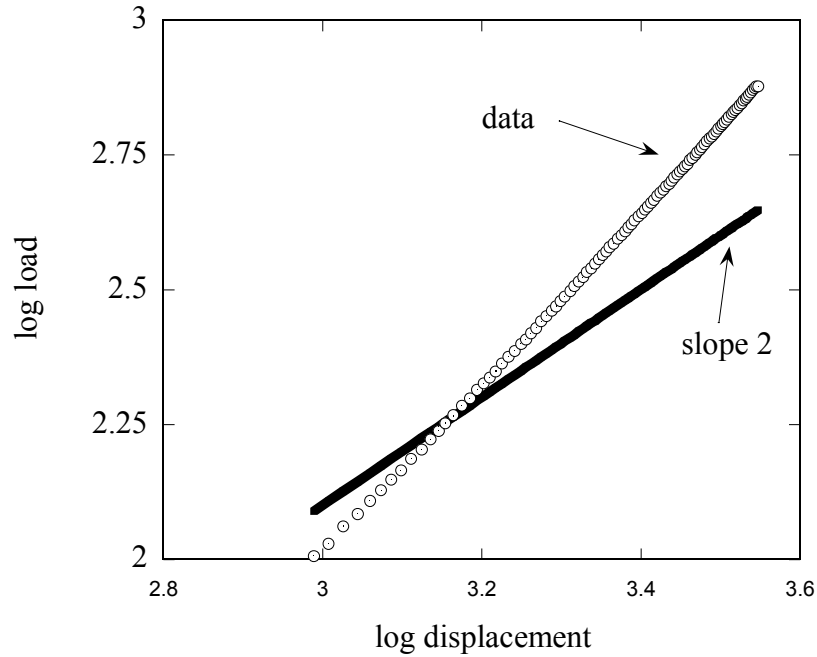
Figure 5-12: Log load (P) against log displacement (h) for the loading portion of the P-h response from the sharp Berkovich indenter.
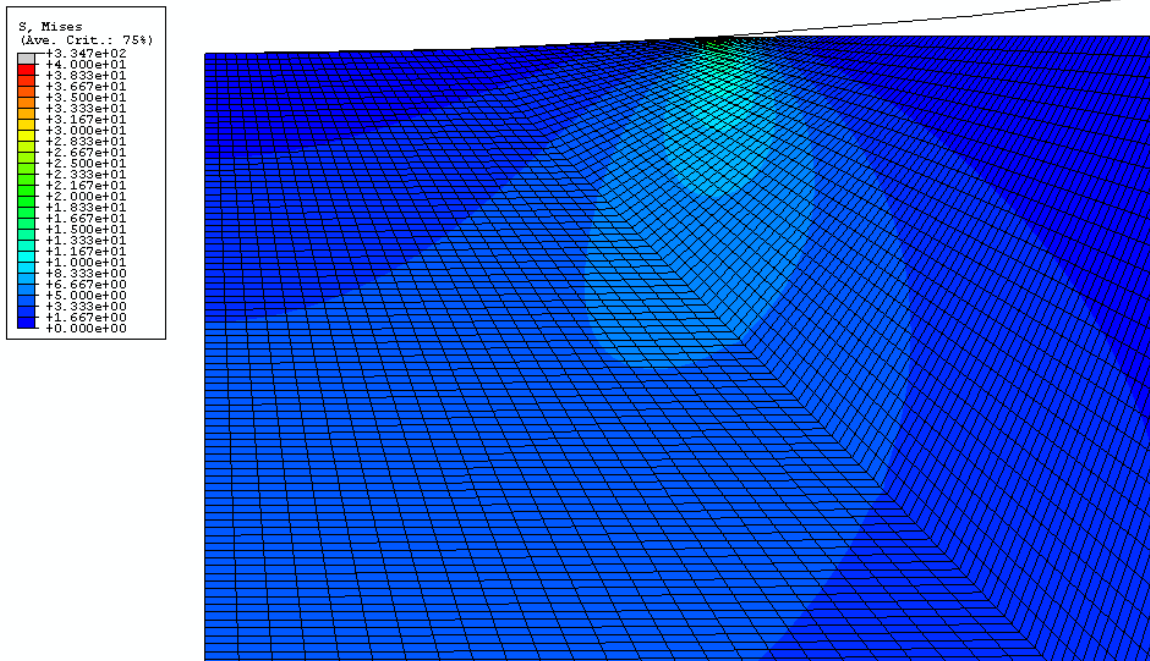
Figure 5-13: The stress contours from the FE model, for the case of a spherical indenter indenting a spherical cavity.

6. STUDY OF DEFORMATION BEHAVIOR OF SUPERELASTIC NiTi USING INSTRUMENTED INDENTATION

The deformation behavior of superelastic NiTi was studied using instrumented nanoindentation with custom diamond spherical indenters. An attempt was made to quantitatively correlate the nanoindentation response to the macroscopic stress strain response. The effect of mechanical cycling on the deformation behavior of the NiTi sample was studied by indenting at the same location to a constant peak load. Indentation experiments with a standard sharp Berkovich indenter were also performed and results were compared with the nanoindentation response obtained with the spherical indenter. The elastic modulus value for the austenite from spherical indentation was found to be 62 GPa and this value increased with cycling while there was a substantial decrease in the hysteresis.

6.1 **Background**

Nickel rich near equi-atomic NiTi shape memory alloys exhibit a deformation mechanism that is known as superelasticity. Here, at room temperature and under the influence of applied stress the high symmetry cubic austenite phase (B2) transforms to a low symmetry martensitic phase (B19') and in the process can accommodate strains of up to 8 %. This process is reversible i.e., the martensite reverts back to austenite spontaneously, upon removal of applied stress[26,27]. In many engineering applications[50], including biomedical devices[51] such as rotary dental drills that make use of superelastic NiTi , repetitive loading and unloading results in forward and reverse austenite-martensite transformation; and the associated changes in the stress-strain response of a superelastic NiTi are well documented in the literature[52-57]. While instrumented indentation has been used previously to study the deformation behavior of SMAs[37-39,45,58,59], mechanical cycling

and associated changes in the stress strain behavior of a superelastic NiTi have not been investigated using instrumented indentation, to the best of the author's knowledge. Instrumented indentation offers a novel way of studying the changes associated with the mechanical cycling of a superelastic NiTi and is advantageous over other techniques primarily because of its ability to assess small sampling volumes and relative simplicity. This makes it a very cost effective quality control tool that can be employed on a day-to-day basis.

In the previous chapter a methodology to extract the mechanical properties of a material using spherical indentation that is applicable to materials with alternative deformation mechanisms such as twinning was detailed and exemplified for the case of a shape memory (Ti-rich) NiTi. In this study, the same methodology has been extended to superelastic NiTi (Ni-rich) to:

i. study the deformation behavior using instrumented indentation, namely – determine the elastic modulus of the parent austenite before it transforms to martensite under the application of stress from the nanoindentation response, identify onset of events like stress induced martensite transformation and elastic deformation of the stress induced martensite transformation;

ii. study the effect of mechanical cycling on the elastic modulus of the austenite, the hysterisis i.e., the area between the loading and the unloading portion of the P-h curve; and

iii. try to correlate the nanoindentation response to the macroscopic stress strain response.

A typical macroscopic stress strain response obtained using an extensometer for superelastic NiTi showing different regions of deformation is illustrated in figure 6-1.

6.2 **Materials and Methods**

The details of sample fabrication have been described in previous chapters and only a summary is presented here. The superelastic NiTi investigated in this work (51.0 at. % Ni) was fabricated from pre-alloyed NiTi powders subjected to hot isostatic pressing (HIP) and subsequently solutionized at 1000 $^{\circ}$C for 1 hour and oil-quenched to room temperature in titanium gettered flowing argon, annealed at 400 $^{\circ}$C for 1 hour and quenched in ice water . The lack of texture in the sample was also previously confirmed[57].

A Nanotest 600 (Micromaterials Limited, Wrexham UK) was used to indent the above sample. A custom 2.0 mm diameter diamond spherical indenter, figure 6-2, was used for the indentation experiments and all indentation experiments were performed at room temperature. A spherical indenter was preferred as the primary indenter over a sharp indenter for the same reason as before - in order to obtain a non-singular stress field under the indenter and delay the onset of stress induced martensite transformation and plastic deformation. The machine compliance was estimated and verified as reported in the previous chapter.

Initially, indents to maximum loads of 3 N, 7 N and 19 N were made on the virgin surface to primarily study the nanoindentation response of the superelastic NiTi and subsequently relate it to its macroscopic response. Thereafter repeated indents to a maximum load of 19 N were made at the same location. A total of 70 repeated indents were made at each location with complete unloading between two consecutive indents. A loading rate of 150 mN/s was used for all spherical indentation experiments. The Hertzian analytical solution for a spherical indenter indenting a flat surface was used to extract elastic properties such as the Young's modulus as

explained previously for the case of shape memory NiTi. The maximum shear stress under the indenter, τ_{max}, was estimated using the following expression:

$$\tau_{max} = 0.31 \left(\frac{6PE^{*2}}{\pi^3 R^2} \right)^{1/3}$$

5-2

where P is the load, E* is a reduced elastic modulus that accounts for non-rigid indenters and R is the radius of the indenter.

Sharp indentation experiments were also performed using a standard Berkovich indenter at a loading rate of 75 mN/s. The results thereof are compared with those from spherical indentation in a following section.

Finite element modeling was employed to analyze load depth responses from indentations at the same location as explained in detail in a later section.

6.3 Results

6.3.1 Spherical Indentation

Indentations made on the virgin surface were analyzed to study the deformation behavior of the specimen. Accordingly, the nanoindentation response on a virgin surface of the superelastic NiTi specimen is presented in figure 6-3a. The P-h curves corresponding to maximum loads of 3 N, 7 N and 19 N are shown. For the loading portion of these P-h curves, log P was plotted against log h as shown in figure 6-4, to distinguish between elastic and inelastic deformation. The Hertzian solution predicts a 3/2 power law P-h response for the elastic deformation of a flat surface

indented by a sphere[11,44]. Consequently, when log P for the loading portion of a P-h response is plotted against log h any inelastic response will not follow a 1.5 slope and thus can be distinguished from elastic deformation. No such deviation from the 1.5 slope and thus no inelastic deformation is observed in figure 6-4a i.e. the deformation observed when the NiTi specimen was loaded up to 3 N and this indicates predominantly elastic deformation of austenite prior to stress induced martensite transformation. In figure 6-4b, however, where the log P vs log h plot for the loading portion corresponding to a 7 N indent is shown, a deviation from the 1.5 slope is clearly observed and this indicates the onset of large scale stress induced martensite transformation. The fact that this is indeed stress induced martensite transformation and not plastic deformation is confirmed from the log P versus log h plot for the loading portion of the 19 N P-h curve, whereupon we see the data reverting back to a 1.5 slope that indicates the elastic deformation of the stress induced martensite phase. Having differentiated between elastic and inelastic deformation thus, the elastic modulus for the parent austenite phase was determined by a 3/2 power fit to the loading portion of the predominantly elastic 3 N P-h curve, as shown in figure 6-5. From the resulting C value, an elastic modulus value of 62 ± 1.2 GPa was obtained using the Hertzian equation as was demonstrated for the case of shape memory NiTi earlier. The reported values are from 20 comparable curves. The maximum shear stress under the indenter at the point of deviation from a 1.5 slope was estimated using the expression from equation 6-1. For the case shown in figure 6-4c values of 222 MPa and 557 MPa were obtained corresponding to the points B and C in figure 6-1.

P-h responses from repeated indentations at the same location to the same maximum load of 19 N as shown in figure 6-3b, analogous to mechanical cycling, were analyzed to study the effect of

cycling on the value of elastic modulus of the austenite and the effect on the hysteresis, which was studied by tracking the area between the loading portion of the P-h curve and the unloading portion of the P-h curve as well as the residual depth. The variation in the elastic modulus of the austenite is presented in figure 6-6 and an initial increase followed by an apparent stabilization is observed. The modulus in this case was determined by fitting a 3/2-power law to the initial elastic portion of the P-h curve. The effect of cycling on residual depth and hysteresis is shown in figures 6-7 and 6-8 respectively. A substantial drop in both the residual depth and the hysteresis with cycling was observed as is evident from the figures.

6.3.2   Sharp Indentation

Figure 6-9 shows P-h responses obtained using a standard sharp Berkovich indenter to two different maximum loads of 750 mN and 3.5 N. Elastic modulus values of the material were obtained from the slope of the initial unloading portion of these curves using the analysis procedure proposed by Oliver & Pharr[9]. A value of 75 $\pm$ 1.5 GPa was obtained for the elastic modulus of the material, from 20 comparable curves. It was not possible to distinguish between elastic and inelastic deformation here, as was done for the case of spherical indentation. For the elastic loading of a flat surface using a Berkovich indenter, the relationship between the load (P) and depth (h) is given by[7,49]

$$P = Ch^2 = 2.1891(1 - 0.21\nu_i - 0.01\nu_i^2 - 0.41\nu_i^3)E^*h^2 \qquad\qquad 2\text{-}1$$

where E* is the reduced modulus described earlier and ν_i is the Poisson's ratio of the indented material. Hence to isolate the elastic deformation and estimate the elastic modulus using the above expression, the log P for the loading portion of the curve was plotted against the

corresponding log h as presented in figure 6-10. However as is evident from the figure the data fits a line with a slope of 2 very poorly. This is attributed to the early onset of plastic deformation in the case of a sharp indenter because of the inherently higher magnitude of stresses under a sharp indenter. This relegates events like elastic deformation and subsequent stress induced martensite transformation to very small loads.

6.4   Discussion

It is evident from the above results that the deformation behavior of the superelastic NiTi can be mapped accurately using instrumented indentation. The elastic modulus value of about 62 GPa obtained for the parent austenite phase here is closer to the value of about 71 GPa reported from neutron diffraction measurements earlier[33]. The elastic modulus value from indentation is closer to the value from neutron diffraction measurements than the 50 GPa reported from a conventional extensometer[33]. While the technique of neutron diffraction inherently measures elastic strain (as opposed to non-elastic strains which can only be measured when they influence elastic strains) and is not expected to be significantly influenced by any limited stress induced martensite transformation at low stresses and thus yields a higher and a more representative elastic modulus value, it is interesting to examine why instrumented indentation yields a value higher than that reported by an extensometer. For this, consider that the in-plane shear stress under a spherical indenter is maximal at a ratio of depth to indenter contact half-width of 0.48, and not directly below the indenter[44]. The surrounding material at this depth can spatially constrain transformation at low stresses. Martensite transformation does eventually occur but at higher stresses as was shown for the case of twinning in shape memory NiTi. In the case of the extensometer, small inelastic strains from martensite transformations at low stresses are

65

indistinguishable from plastic strains and this results in a deflated elastic modulus. It was shown that even a 1 vol. % martensite transformation can result in a substantially deflated elastic modulus value from an extensometer[57].

The fact that no deviation from a 1.5 slope is observed in figure 6-4a indicates a predominantly elastic deformation of the parent austenite. This corresponds to the region AB in figure 6-1. Subsequently when the specimen is indented to a maximum load of 7 N a deviation from the 1.5 slope is observed from the log P versus log h plot as shown in figure 6-4b. This corresponds to approximately point B on figure 6-1. The maximum shear stress under the indenter at this point was calculated to be 348.5 MPa for the graph shown in figure 6-4b. This value of stress cannot be directly compared to the uniaxial stress at B in figure 6-1 because the former is multiaxial in nature; an outcome of the stress state under the indenter being multiaxial. Subsequently when the specimen is loaded up to a maximum load of 19 N, the corresponding P-h curve (loading portion) reverts back to a 1.5 slope, which indicates that the deformation after the reversion is predominantly elastic and represents the elastic deformation of stress induced martensite. Therefore, it can be concluded that the small amount of residual depth associated with the first P-h curves corresponding to the 19 N maximum load on a virgin surface is probably because of an incomplete reversion of martensite to austenite upon unloading. The maximum stress under the indenter at the point where the data reverts back to the 1.5 slope was calculated to be 557 MPa and this approximately corresponds to C in figure 6-1. Although a direct relation between the maximum shear stresses under the indenter calculated above could not be established because of the different stress state, this information can still be of immense use. For example, when optimizing thermomechanical-processing parameters on centimeter scaled button melts or for

quality control purposes of small volume devices, these stresses can be related to the corresponding transformation temperatures through the Classius-Clapeyron equation.

The effect of mechanical cycling on the nanoindentation behavior was studied by analyzing the data from indentations at the same location as described in an earlier section. It was also shown that the residual depth in the first P-h response from a virgin surface was not because of plastic deformation. This is further corroborated by figure 6-7 where we see a drop in residual depth with subsequent indents at the same location. This drop could only be because of mechanical cycling brought about by repeated indentations at the same location, that stabilizes the austenite-martensite transformation as well as increases the volume fraction of the stress induced martensite volume fraction; as was shown earlier for the same specimen using neutron diffraction[57]. The stabilization of the martensitic transformation in this study is evident from figures 6-8 and 6-6. In figure 6-8 a drop in the measured hysteresis (area between the loading and unloading curve) is observed and in figure 6-6 an increase in the measured elastic modulus is observed. The elastic modulus calculations from P-h curves of indents at the same location were made using the Hertzian analysis. However it was shown earlier for the case of shape memory NiTi in chapter 5 that indentations at the same location can result in a situation where indents are not made on a flat surface thereby rendering the property estimation using Hertzian formulation erroneous and resulting in a stiffer P-h response. In this study the residual depth at the end of the first indent indicates that the subsequent indents at the same location can possibly be on the cavity from the first indent. Hence, to verify that the increase in elastic modulus observed in figure 6-6 is indeed because of mechanical cycling and not due to the aforementioned geometrical effect, finite element modeling was employed. The profile of the surface after 60

indents was measured using the nanoindenter as a profilometer and the result is presented in figure 6-11. The depth of the cavity was thus determined to be about 750 nm. This profile was modeled in SRDC I-DEAS and was subsequently translated into ABAQUS[48] and indentation simulations using a rigid indenter were executed in ABAQUS as detailed earlier for the case of shape memory NiTi. The Poisson's ratio used for the material was 0.35 (ref. [41]). The resulting P-h curve is compared with the one from a flat surface as shown in figure 6-12. As is evident from this figure the size of the cavity resulting from repeated indentations is not sufficient to inflate the modulus to levels observed here. Hence, it can be concluded that the increase in the elastic modulus is solely because of the austenite-martensite transformation stabilization and an increase in the volume fraction of the stress induced martensite.

The elastic modulus value of about 75 ± 1.5 GPa obtained from sharp indentation is higher than what was obtained from spherical indentation. For the case of superelastic NiTi, the unloading slope also includes recovery by way of reverse transformation and elastic recovery of the elastically deformed martensite and parent austenite[38]. That this is indeed the case here is evident from the relatively large residual depth and thus plastic deformation associated with the P-h curves from sharp indentation in figure 6-9, since large scale plastic deformation is possible only after stress induced martensite transformation. Consequently the resulting elastic modulus value is convoluted and is not solely representative of the austenite. Hence, it cannot be compared with values for austenite from spherical indentation or neutron diffraction measurements.

6.5   Conclusion

The following conclusions can be drawn from the present study:

i.   the elastic modulus of austenite prior to the onset of stress induced martensite was found to be about 62 GPa from spherical indentation which is closer to the value of 71 GPa from neutron diffraction measurements than the 50 GPa from extensometry;

ii. onset of large scale stress induced martensite transformation was successfully identified from the nanoindentation response and the elastic deformation of the stress induced martensite was identified by the double 3/2 slope in the P-h response;

iii. mechanical cycling increases the elastic modulus of the parent austenite and the associated hysteresis due to the austenite-martensite transformation stabilization with cycling;

iv. sharp indentation gives a overall elastic modulus of about 75 GPa for the material and is not phase specific; and

v.   the nanoindentation response has been partially correlated to the macroscopic stress strain response.

6.6 Figures
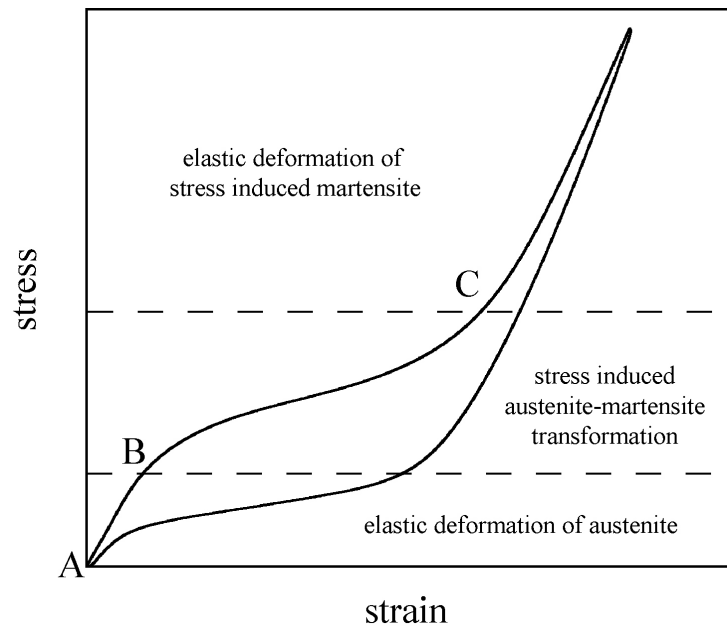
Figure 6-1: A typical macroscopic stress strain response of superelastic NiTi showing different deformation regions.
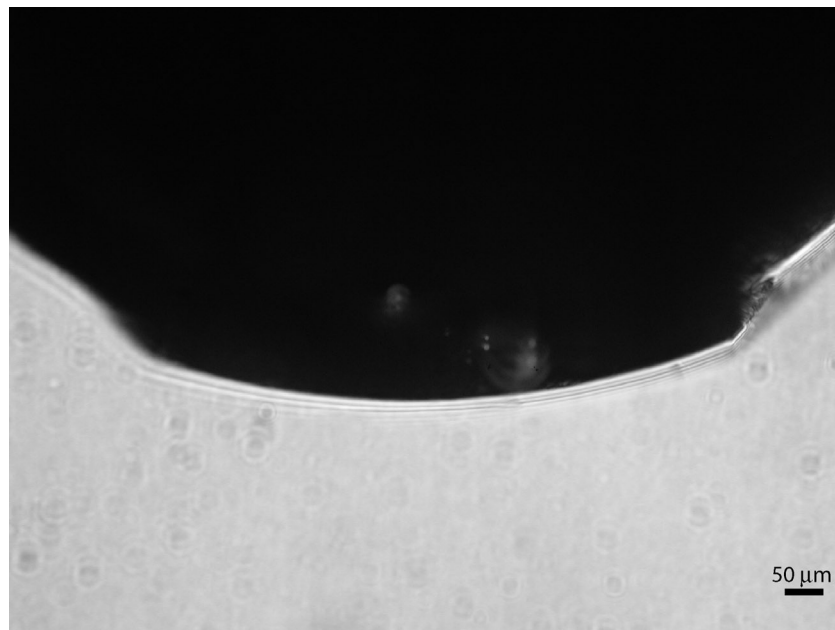
Figure 6-2: The 2.0 mm custom-made diamond spherical indenter used for spherical indentation in this study.
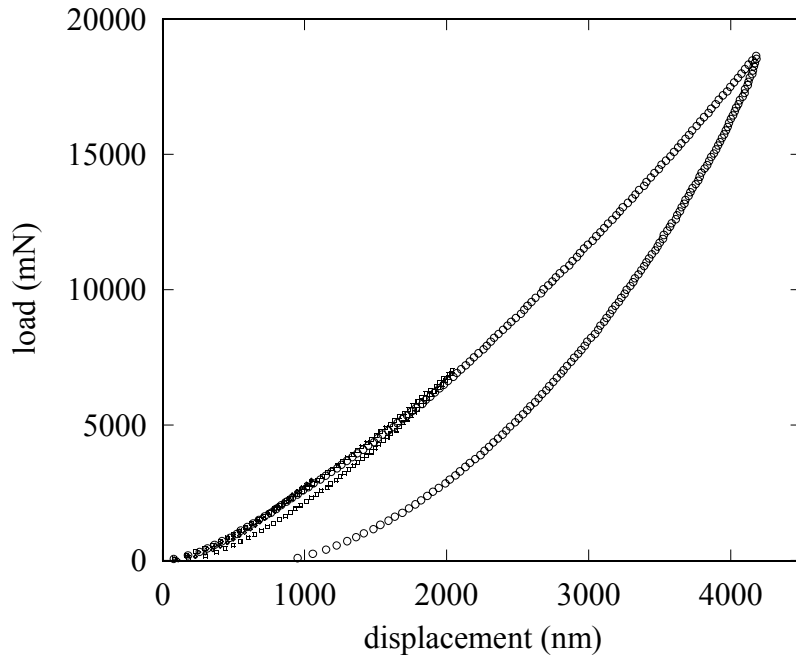
Figure 6-3a: Representative P-h curves from indentation of a virgin surface on the superelastic NiTi specimen, loaded to maximum loads of 3 N, 7 N and 19 N.
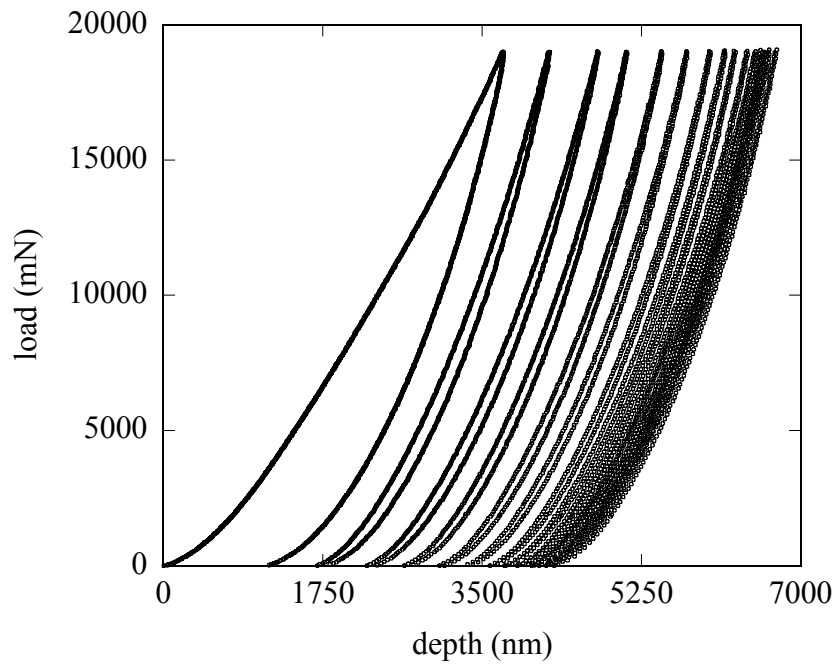
Figure 6-3b: P-h curves from 70 repeated indents at the same location to a maximum load of 19 N. For the sake of clarity every fifth indent is shown here.

Figure 6-4a: Log load (P) against log displacement (h) for the loading portion of the P-h response corresponding to a maximum load of 3 N.

Figure 6-4b: Log load (P) against log displacement (h) for the loading portion of the P-h response corresponding to a maximum load of 7 N.
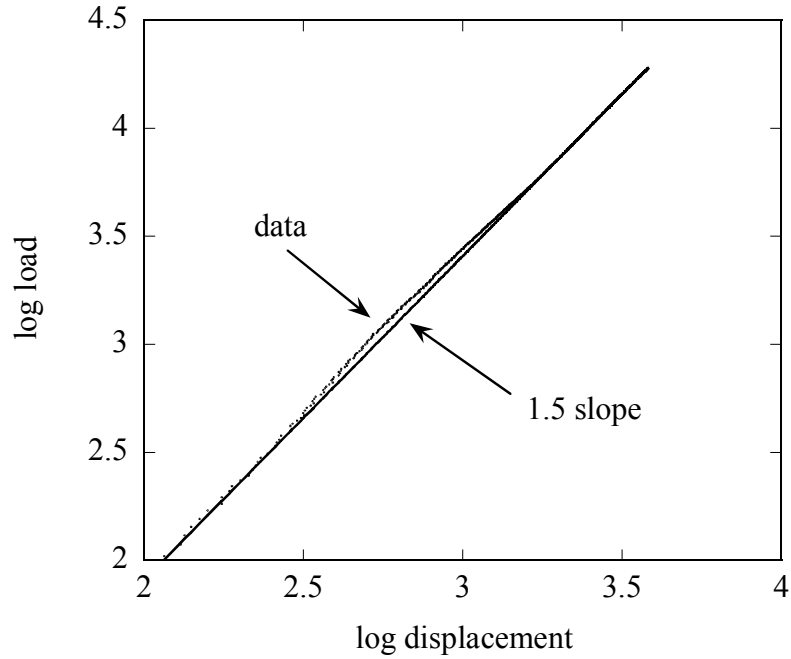
Figure 6-4c: Log load (P) against log displacement (h) for the loading portion of the P-h response corresponding to a maximum load of 19 N.
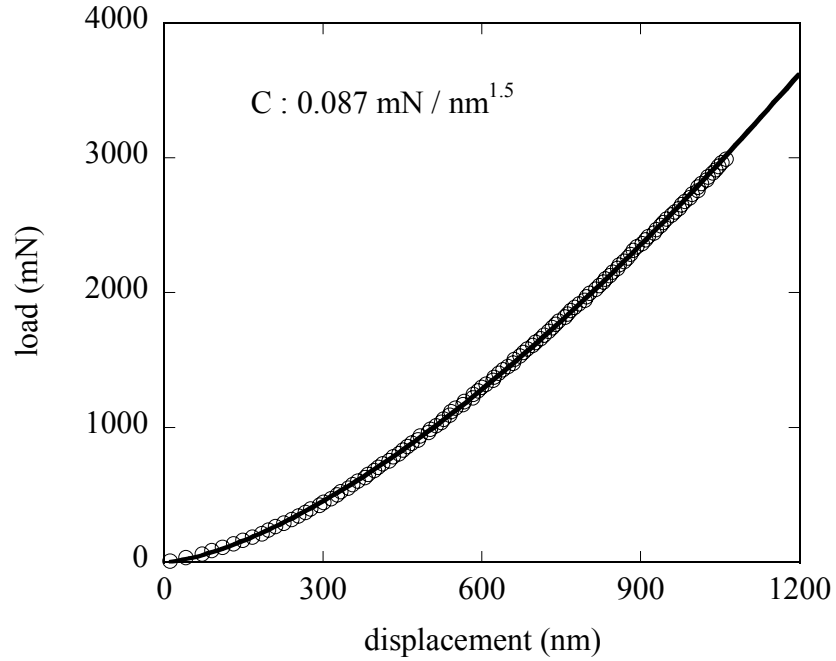
Figure 6-5: 3/2 power fit to the loading portion of a 3 N P-h curve.
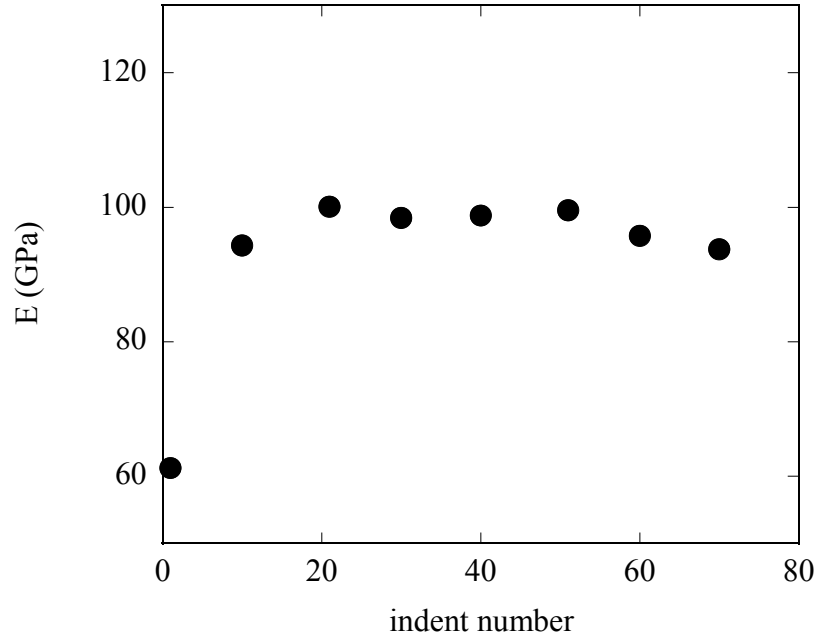
Figure 6-6: The elastic modulus variation with mechanical cycling resulting from repeated indents at the same location. The increase in modulus after the first ten cycles is because of stabilization of residual martensite.
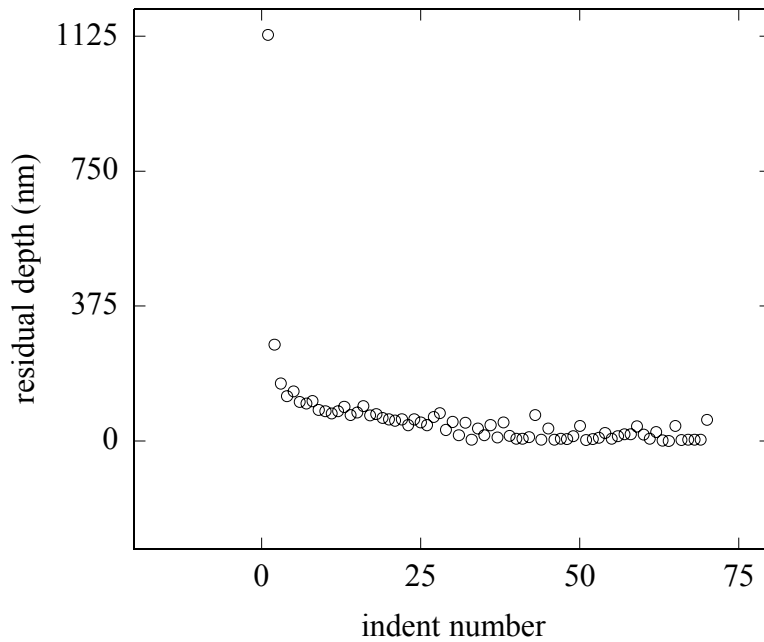
Figure 6-7: The variation in residual depth with mechanical cycling resulting from repeated indents at the same location. The drop in residual depth after the first cycle is because of martensitic transformation stabilization after the first cycle.
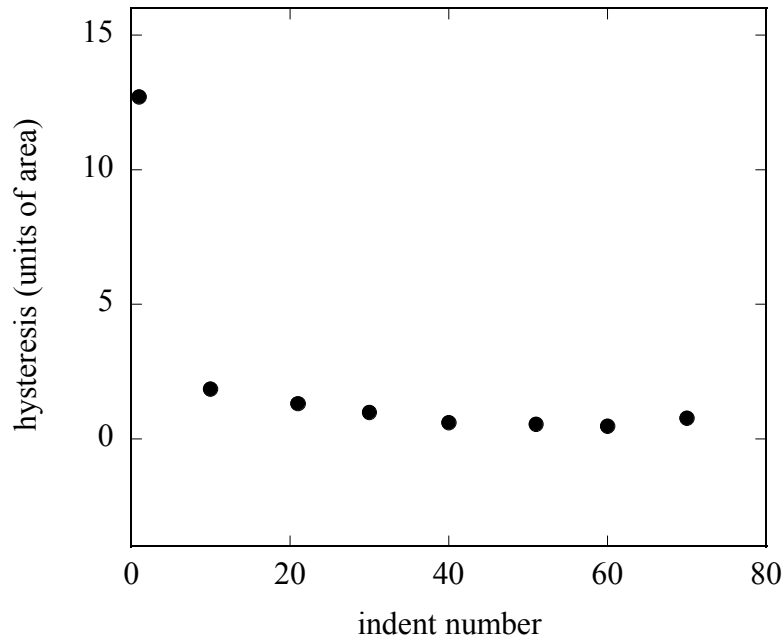
Figure 6-8: The variation in hysteresis with mechanical cycling resulting from repeated indents at the same location. The drop in hysteresis after the first ten cycles is because of martensitic transformation stabilization.
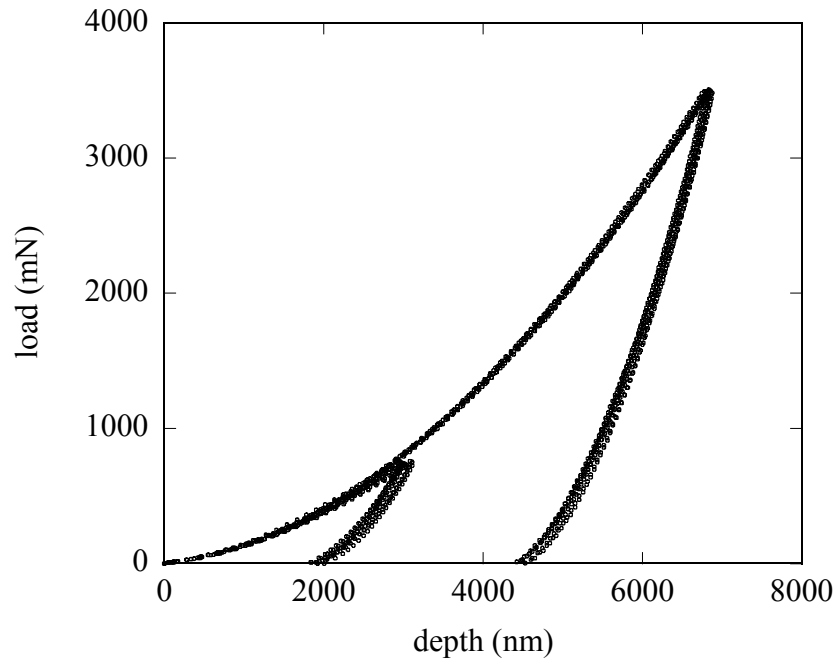
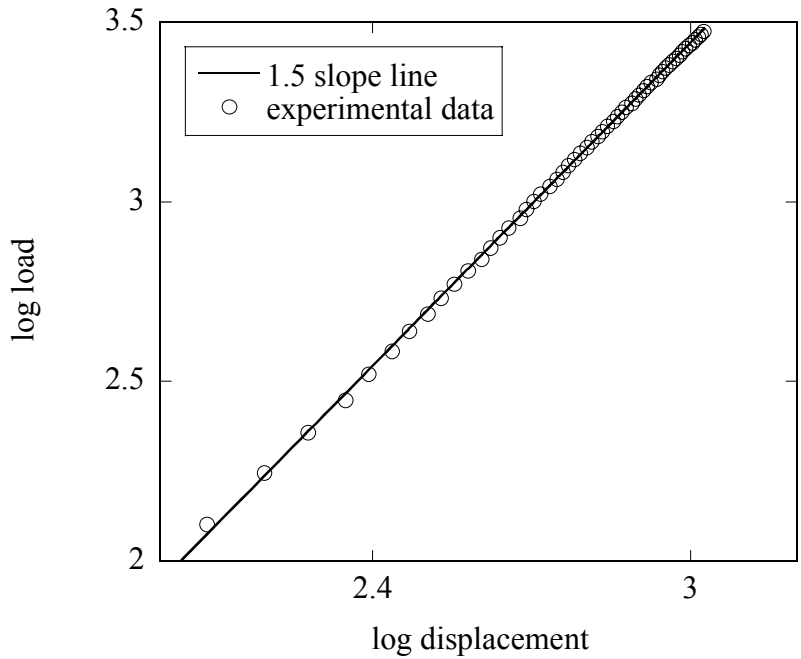Figure 6-9: P-h curves corresponding to 750 mN and 3.5 N sharp Berkovich indents.

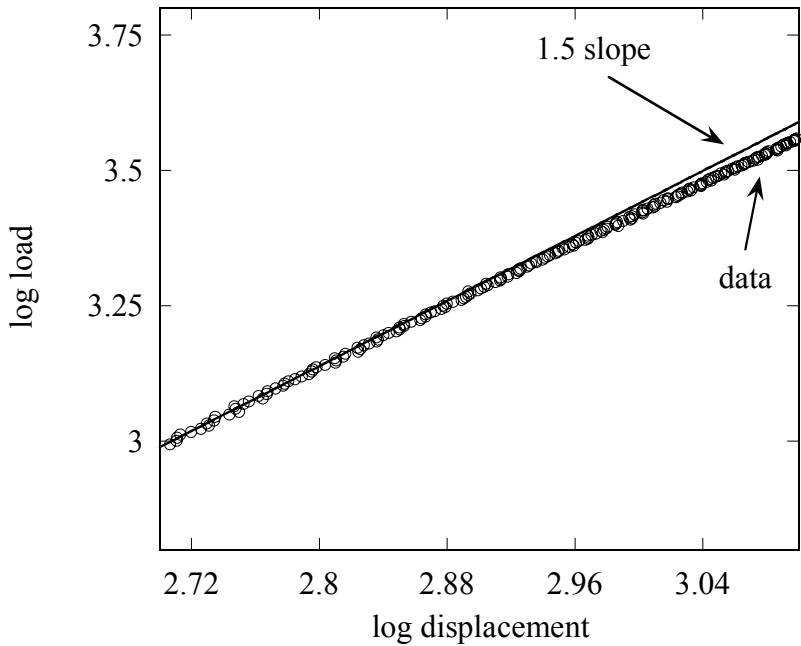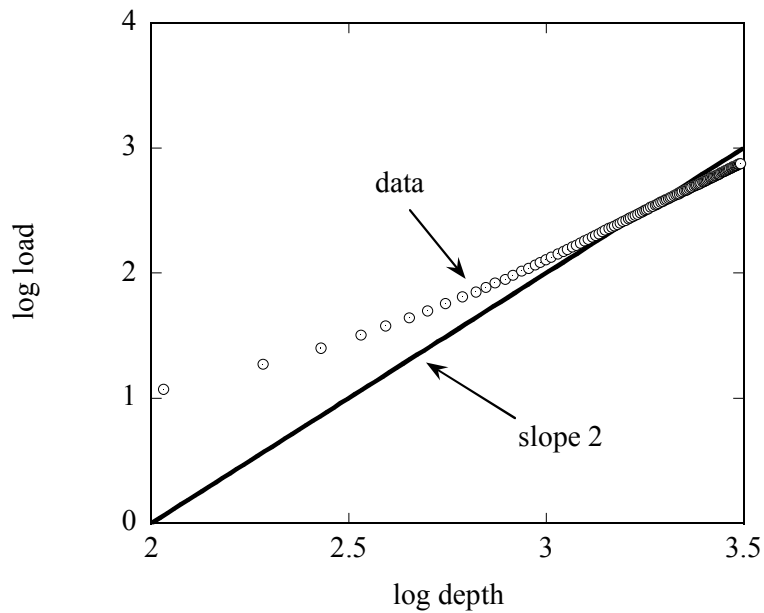Figure 6-10: Log load (P) against log displacement (h) for the loading portion of the P-h response corresponding to a maximum load of 750 mN from sharp indentation.
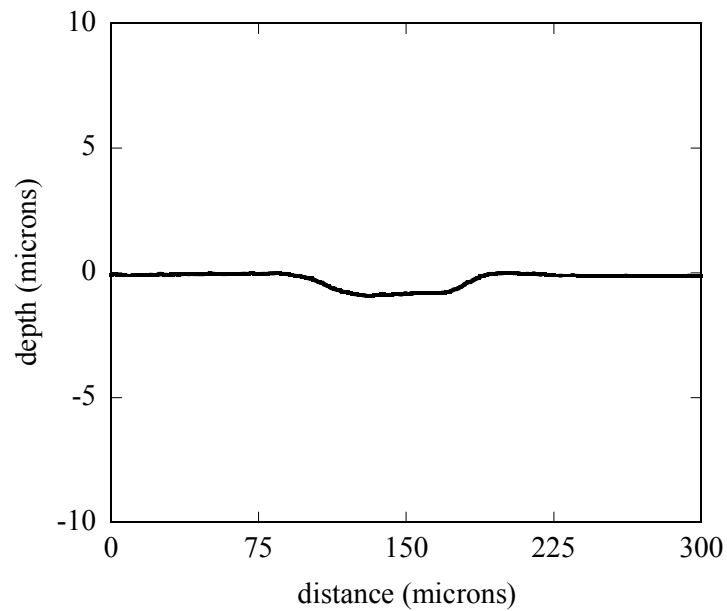
Figure 6-11: The profile of the surface after 60 repeated indents were made to the same maximum load of 19 N.
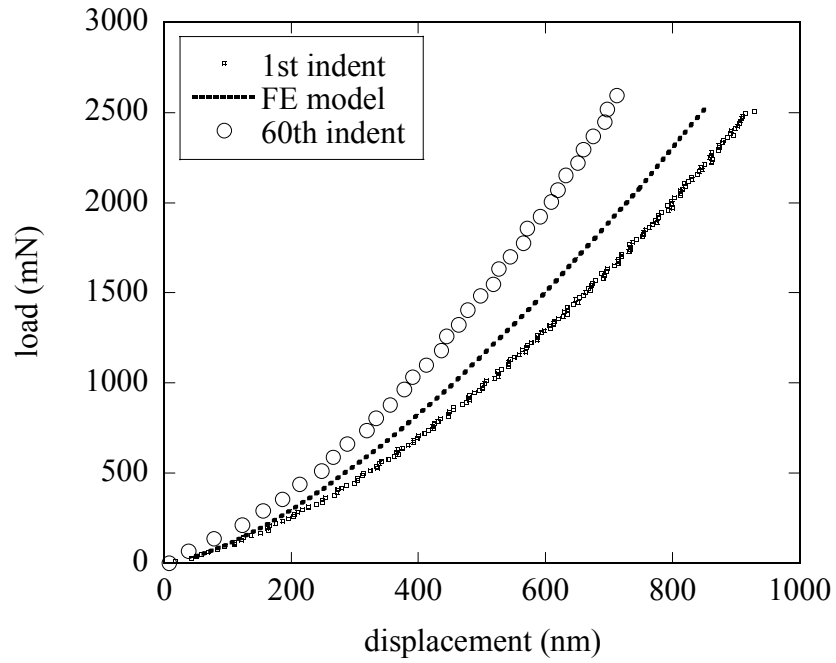
Figure 6-12: The p-h curves corresponding to the first and the 60th indent at the same location plotted along side the FEM prediction for indenting a cavity of 750 nm with the 2.0 diamond spherical indenter.

7. INSTRUMENTED INDENTATION OF CARBON NANOTUBE REINFORCED POLYMER-DERIVED CERAMIC COMPOSITES

The effect of carbon nanotube (CNT) content on the mechanical properties of a polymer-derived ceramic composite was studied using instrumented indentation. Three different samples with 0 vol. %, 1.3 vol. % and 6.4 vol. % CNT content respectively were tested. The elastic moduli of the three samples were measured using a diamond spherical indenter and the hardness was measured using a standard sharp Berkovich indenter. Both, the elastic modulus as well as the hardness increased with increasing CNT content.

7.1 Background

Carbon nanotubes have attracted tremendous interest in the last decade because of their superior properties. Theoretical and experimental studies have shown that single-walled carbon nanotubes (SWCNTs) possess Young's moduli of the order of 1-5 TPa[60-63] and tensile strengths as high as 60 GPa[64,65]. Depending on their diameters and orientations of their hexagons with respect to their tube axes, CNTs can be either semiconducting or metallic[66,67]. The axial thermal conductivity of CNTs is higher than even that of diamond. These unique properties suggest that CNTs hold great promise for synthesizing new kinds of multifunctional nanocomposites. As for their use in ceramic-matrix composites, at least two can be conceived: i) CNTs can be used as reinforcements to improve mechanical properties and add new functionality, and ii) ceramic matrices can be used to protect functional CNT structures from harsh environments. The ceramic-matrix composites are potentially important for those applications where requirements such as mechanical strength or resistance to corrosive environments prevent the use of other matrices such as polymers and metals.

Instrumented indentation is ideally suited for assessing the mechanical properties of these composites again because of the small sampling volumes involved, as is shown in a later section and analogous to the case of shape memory alloys, samples with varying compositions can be tried before large-scale production.

7.2 <u>Materials and Methods</u>

In this study, two composites containing SiCN-1.3 vol. % CNTs and SiCN-6.4 vol. % CNTs respectively, were tested using instrumented indentation. For comparison, a monolithic ceramic without CNT additives (SiCN-0 vol.% CNTs) was also tested (synthesized under the same processing conditions). The samples were about 4.0-10.0 mm in diameter and about 1.5–2.0 mm in thickness as shown in figure 7-1. These specimens were not synthesized as part of the author's doctoral work and further details about their processing methodology is available in ref. 6.

A Nanotest 600 (Micromaterials Limited, Wrexham UK) was used to indent the above samples. A custom 100 μm diameter diamond spherical indenter was used for the indentation experiments and all indentation experiments were performed at room temperature. A sharp Berkovich indenter was used to measure the hardness of the samples. A total of 15 indents were made on each sample with each indenter. A loading rate of 75 mN/s was used for both the spherical indentation and sharp indentation experiments.

The spherical indentation data were analyzed using the Hertzian analytical solutions as described previously to obtain the Young's moduli of the specimens and the procedure proposed

by Oliver & Pharr[9] was used to determine the hardness of the specimens from the sharp indentation data.

7.3 Results

The spherical nanoindentation results are summarized in figure 7-2 and figure 7-3 is a magnification of the residual deformation associated with each of the specimens. The sharp indentation results are presented in figure 7-4. No "pop-ins", or steps in the load-depth response, indicative of a porous matrix, were observed. More importantly an increase in stiffness and a decrease in residual deformation is observed with increasing CNT content. Using the Hertzian analysis procedure for spherical indentation, the elastic moduli values of the 0 vol.%, 1.3 vol.% and 6.4 vol.% CNTs –polymer derived ceramic composite was found to be 74 GPa, 109 GPa and 118 GPa respectively. The corresponding hardness values from sharp indentation was found to be 9.4 GPa, 10.5 GPa and 14.3 GPa respectively.

7.4 Discussion

The indentation results indicate that the stiffness of the composites increased with increasing CNT content. More significantly, the residual deformation decreases with increasing CNT content - in particular, the composite containing 6.4 vol.-% CNTs showed almost no residual deformation, suggesting remarkable improvement in contact-damage resistance. This result is rather surprising since the P-h curve of the 6.4 vol.-% CNT composite clearly shows "plastic" deformation (displacement-load curve deviates from Hertzian elastic behavior and small gap between the loading and unloading portions of the P-h curve corresponding to the 6.4 vol.-% CNT composite in figure 7-2). The possible explanation is that the cone cracks formed under

Hertzian indentation were bridged by partially debonded CNTs that deformed elastically. When the applied load was withdrawn, the elastic restoration of the CNTs exerted a closing force on the cracks to restore the deformed material. Further investigation into this issue is ongoing. This result suggests that the composite may possess a significantly high fatigue resistance under localized cycling loads. The low values of Young's modulus and hardness of the monolithic SiCN can be attributed to the presence of hydrogen in the synthesized specimen.

7.5   Conclusions

The nanoindentation tests validated the structural integrity of the fully dense ceramic-CNT composites with homogeneously distributed multi-walled CNTs synthesized by using polymer-derived ceramic composites as matrices. Results further indicate a significant improvement in the mechanical properties, elastic modulus and hardness, with only 6.4 vol.% addition of CNTs.

7.6   Figures

Figure 7-1: CNT-polymer derived ceramic composite specimens subjected to instrumented nanoindentation.
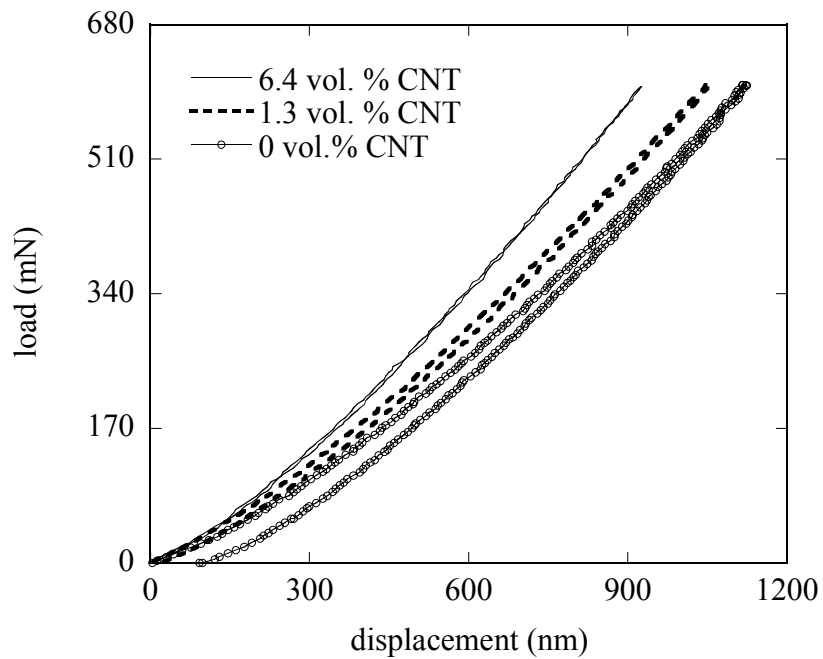
Figure 7-2: Load displacement curves measured using a spherical diamond indenter for a 0 vol.% (monolithic SiCN), 1.3 vol.% and 6.4 vol.% CNT composite.
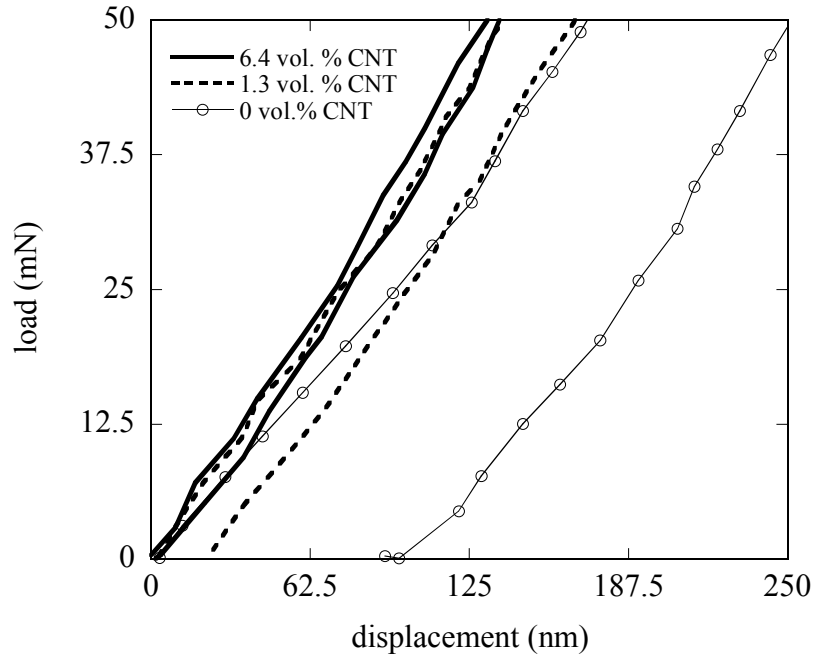
Figure 7-3: Magnification of the bottom left corner of figure 7-2, which shows the permanent deformation on unloading.
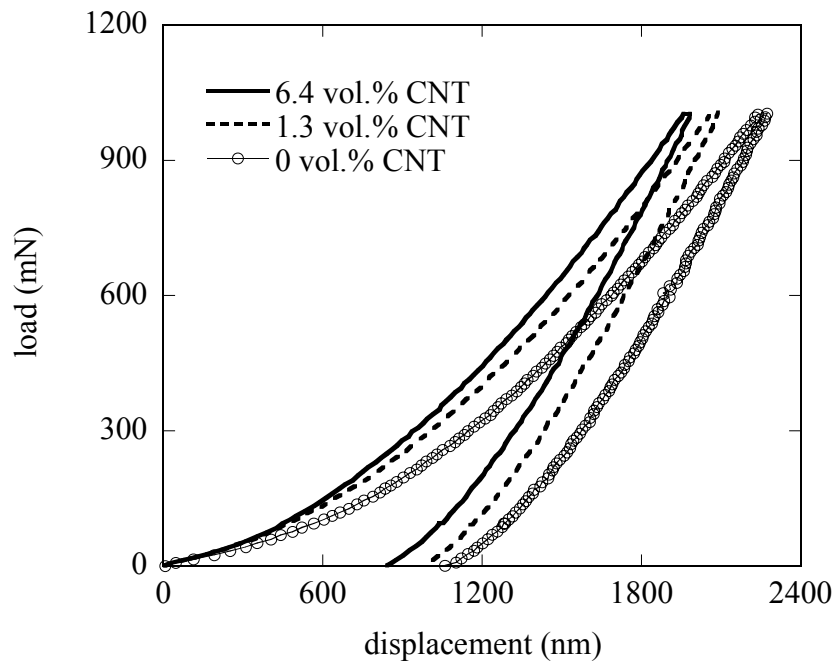
Figure 7-4: Load displacement curves measured using a sharp Berkovich indenter for a 0 vol.% (monolithic SiCN), 1.3 vol.% and 6.4 vol.% CNT composite.

8. CONCLUSIONS

A broader perspective of the results from this work and the overall conclusions that can be drawn thereof are summarized here and some possible directions in which this work can be advanced in the future is listed.

8.1 <u>Summary of Results and Conclusions</u>

Shape memory NiTi

The nanoindentation studies of shape memory NiTi yielded valuable information regarding the elastic behavior of B19' martensite prior to the onset of large-scale twinning. The elastic modulus of the martensite prior to twinning was determined successfully using spherical indentation to be about 101 GPa, which was comparable to the value from neutron diffraction but substantially higher that the extensometer reported value of about 68 GPa. This was shown to be because of twinning at low stresses, which reduces the elastic modulus estimated by an extensometer. Further studies were able to successfully identify the onset of large-scale twinning from the log P versus log h plots. The onset of predominantly elastic deformation of the twinned martensite and the subsequent elastic deformation was observed by indenting at the same location and tracking the residual depth as a function of the maximum load. The elastic modulus of the twinned martensite from the nanoindentation response was estimated to be about 17 GPa and finite element modeling was used to validate the measurements. When compared to the relatively limited amount of previous indentation work[37-39,68,69] on shape memory NiTi the current work has provided for the first time:

i. a means to extract quantitative information related to the deformation behavior of the shape memory NiTi, using spherical indentation as opposed to the largely qualitative nature of the previous studies;

ii. a link between the nanoindentation response and the macroscopic stress strain curve with immediate relevance to optimizing thermomechanical processing parameters in centimeter-scaled button melts prior to large scale production; and

iii. a methodology for selected property extraction using spherical indentation for shape memory alloys.

On the other hand, some of the results from this work are in excellent agreement with what has been reported previously. For example, the deflation of elastic modulus, because of a phase transformation at low stresses, measured using an extensometer was reported for the case of a superelastic NiTi[57] and has been suggested for shape memory NiTi using macroscopic mechanical testing[70]. In this work it was conclusively shown that this is indeed the fact, using instrumented indentation.

Superelastic NiTi

For the case of the superelastic NiTi, the elastic modulus value of the parent austenite was estimated to be about 62 GPa using nanoindentation. The onset of large-scale stress induced martensite transformation and its subsequent elastic deformation was identified from the nanoindentation response. The corresponding maximum shear stresses under the indenter at this point were estimated. Subsequently, the effect of cycling on the mechanical behavior of the NiTi specimen was studied by repeatedly indenting at the same location. An increase in the elastic modulus value for the austenite after the initial few cycles followed by a stabilization was

observed. The effect of cycling on the hysteresis associated with the mechanical behavior was studied by tracking the area between the loading and unloading portion of the curve and the residual depth as a function of the number of cycles. Both showed a sharp decrease in the initial few cycles followed by a stabilization. These results were in good agreement with observations reported for the same material earlier using neutron diffraction[57]. Much of the earlier indentation work associated with superelastic NiTi [37,45,59] involved a sharp indenter and hence not much quantitative information could be obtained as the use of a sharp indenter led to early plasticity, overshadowing events like stress induced martensite transformation. For the case of superelastic NiTi the results from this work are significant because-

  i. it is for first time that phase specific quantitative mechanical behavior information has been obtained using instrumented indentation;

  ii. the nanoindentation response of a superelastic NiTi has been linked to the macroscopic stress strain response with immediate relevance to stent, orthodontic and guide wire geometries; and

  iii. the effect of mechanical cycling on the mechanical behavior has been studied using instrumented indentation.

The study of CNTs reinforced composites, using nanoindentation, validated the novel synthesis methodology and clearly indicated an improvement in the mechanical properties of the composite with increasing CNT content. More importantly, it demonstrated the applicability of the testing methodology developed viz., the compliance calibration and subsequent analysis procedures for property estimation, to other material systems.

8.2   <u>Future Work</u>

The two major areas in which this work can be further advanced is:

i. correlate the maximum shear stresses under the indenter estimated in this work to the corresponding uniaxial stresses in the macroscopic stress strain curves using computational methodologies; and

ii. study of deformation behavior of NiTi SMAs using instrumented indentation at elevated temperatures.

9. APPENDIX - I

FEM / ABAQUS CODES FOR INDENTATION

The following are some of the important issues associated with model generation in I-DEAS, related to this work.

  i. type of elements to be used: quadrilateral axisymmetric.

  ii. connectivity of nodes : always counter-clockwise else the model does not execute in ABAQUS.

  iii. boundary conditions and material information to be specified in ABAQUS and not in I-DEAS.

  iv. the bottom nodes of the blank, the center nodes and the indenter node have to be created and numbered in I-DEAS as shown in figure 9-1

  v. once the model is satisfactory and meets desired dimensions, the model needs to be translated in to ABAQUS standard (option available in I-DEAS).

The following is an example of the finite element code for nanoindentation simulation in ABAQUS, following successful creation of the model in I-DEAS and subsequent translation to ABAQUS standard.

```
**%     ==============================================================
**%
**%                  I-DEAS 9 ABAQUS STANDARD TRANSLATOR
**%                       FOR ABAQUS VERSION 5.8
**%
**%           MODEL FILE: /home4/classes/sp04/eml6067/subha/1mm_400.mf1
**%           INPUT FILE: 1mm_400_3mic.inp
**%             EXPORTED: AT 10:25:04 ON 03-Jun-05
**%                 PART: 1mm_400_3mic
**%                  FEM: 1mm_400_3mic
**%
**%                UNITS: MM-mm (milli-newton)
**%                       ... LENGTH : MM
**%                       ... TIME   : sec
**%                       ... MASS   : kilogram (kg)
**%
**%                       ... FORCE  : milli-newton
**%                       ... TEMPERATURE : deg Celsius
**%           COORDINATE SYSTEM: PART
**%               SUBSET EXPORT: OFF
**%          NODE ZERO TOLERANCE: OFF
**%     ==============================================================
*HEADING
SDRC I-DEAS ABAQUS FILE TRANSLATOR  03-Jun-05   10:25:04
*NODE, NSET=ALLNODES, SYSTEM=R
```

Element Information generated by I-DEAS !

```
*SOLID SECTION,
```

Retain text in the IDEAS generated input file up to this point. Delete text following this point and append the code written below to the input file.

```
 ELSET=ALLELEMENTS,
 MATERIAL=GENERIC_ISOTROPIC_STEEL
*MATERIAL,NAME=GENERIC_ISOTROPIC_STEEL
*ELASTIC,TYPE=ISOTROPIC
 0.20E+05,  3.500E-01     (elastic modulus in N/mm² and Poisson's ratio)
*NSET,NSET=CENTERNODES
25000,25399,1
*NSET,NSET=BOTTOMNODES
25400,25425,1
*NSET,NSET=INDENTERNODE
3000
*************************************************************************
*BOUNDARY              (boundary conditions)
 BOTTOMNODES,1,2
 CENTERNODES,1
 INDENTERNODE,1
 INDENTERNODE,6
*************************************************************************
*SURFACE,TYPE=SEGMENT,NAME=INDENTER  (indenter dimensions)
 START,1.4,2.397
 CIRCL,0.,0.997,0.,2.397
*SURFACE,TYPE=ELEMENT,NAME=BLANK
 ALLELEMENTS,
*RIGID BODY,REF NODE=3000,ANALYTICAL SURFACE=INDENTER
*SURFACE INTERACTION,NAME=INDENT
```

```
*CONTACT PAIR,INTERACTION=INDENT
 BLANK,INDENTER
***********************************************
*STEP,NLGEOM  (indentation simulation)
*STATIC
0.01,1,0.01,0.01
*BOUNDARY
INDENTERNODE,2,2,-0.0003
*END STEP
```
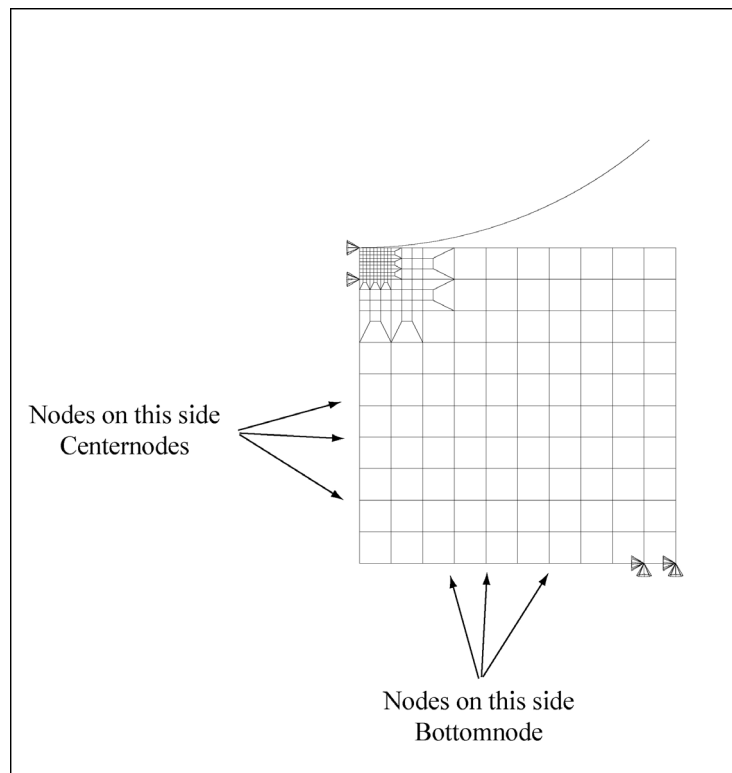
9.1 Figures

Figure 9-1: Illustration of a model used in this work showing node identification

REFERENCES

1. S. Rajagopalan and R. Vaidyanathan, JOM - J. Min. Met. Mat. S. **54** (9), p. 45 (2002).

2. C. R. Rathod, S. Rajagopalan and R. Vaidyanathan, *Mechanical Characterization of Shape-Memory Alloys using Diffraction and Instrumented Indentation*. (Shape Memory and Super Elastic Technologies, 2003), p.331.

3. S. Rajagopalan, A. L. Little, M. A. M. Bourke and R. Vaidyanathan, Appl. Phys. Lett. **86** (8), p. 081901 (2005).

4. S. Rajagopalan and R. Vaidyanathan, J. Biomed. Mater. Res. (To be submitted), (2005).

5. S. Rajagopalan and R. Vaidyanathan, J. Biomed. Mater. Res. (To be submitted), (2005).

6. L. N. An, W. X. Xu, S. Rajagopalan, C. M. Wang, H. Wang, Y. Fan, L. G. Zhang, D. P. Jiang, J. Kapat, L. Chow, B. H. Guo, J. Liang and R. Vaidyanathan, Adv. Mater. **16** (22), p. 2036 (2004).

7. P-. L. Larsson, A. E. Giannakopoulos, E. Soderlund, D. J. Rowcliffe and R. Vestergaard, Int. J. Solids Struct. **33** (2), p. 221 (1996).

8. M. F. Doerner and W. D. Nix, J. Mater. Res. **1** (4), p. 601 (1986).

9. W. C. Oliver and G. M. Pharr, J. Mater. Res. **7** (6), p. 1564 (1992).

10. A. E. Giannakopoulos and S. Suresh, Scripta Mater. **40** (10), p. 1191 (1999).

11. J. Alcala, A. E. Giannakopoulos and S. Suresh, J. Mater. Res. **13** (5), p. 1390 (1998).

12. S. Timoshenko and J. N. Goodier, *Theory of Elasticity*. (McGraw-Hill, New York, 1951).

13. D. Tabor, *Hardness of Metals*. (Clarendon Press, Oxford, United Kingdom, 1951).

14. A. L. Norbury and T. Samuel, Iron and Steel Inst. **17**, p. 673 (1928).

15. D. S. Harding, W. C. Oliver and G. M. Pharr, in *Thin Films: Stresses and Mechanical Properties V, MRS Symposium Proceedings*, edited by P. B. Shefford, A. R. Caroline, H. T. Paul, A. V. Cynthia and B. Peter (Materials Research Society, 1995), Vol. 356, p. 663.

16. M. J. Mayo and W. D. Nix, Acta Metall. Mater. **36** (8), p. 2183 (1988).

17. S. Suresh and A. E. Giannakopoulos, Acta Mater. **46** (16), p. 5755 (1998).

18. C. Larsson and M. Oden, Mater. Sci. Eng. A **382** (1-2), p. 141-149 (2004).

19. R. Vaidyanathan, M. Dao, G. Ravichandran and S. Suresh, Acta Mater. **49** (18), p. 3781 (2001).

20. A. Gouldstone, H. J. Koh, K. Y. Zeng, A. E. Giannakopoulos and S. Suresh, Acta Mater. **48** (9), p. 2277-2295 (2000).

21. L. C. Chang and T. A. Read, Trans. AIME **47**, p. 191 (1951).

22. W. J. Beuhler, J. V. Gilfich and R. C. Wiley, J. Appl. Phys. **34**, p. 1475 (1963).

23. W. B. Cross, A. H. Kariotis and F. J. Stimler, Report No. CR-1433, NASA, (1969).

24. C. M. Jackson, H. J. Wagner and R. J. Wasilewski, Report No. SP-5110, NASA, (1972).

25. R. J. Wasilewski, S. R. Butler and J. E. Hanlon, Met. Sci. **J1**, p. 104 (1974).

26. T. W. Duerig, K. N. Melton, D. Stoeckel and C. M. Wayman, *Engineering Aspects of Shape Memory Alloys*. (Butterworth-Heineman Ltd., Essex, 1990).

27. H. Funakubo, *Shape Memory Alloys : Vol-1:Precision Machinery and Robotics*. (Gordon and Breach Science Publishers, New York, 1987).

28. C. Mavroidis, C. Pfeiffer and M. Mosley, in *Automation, Miniature Robotics and Sensors for Non-destructive Testing and Evaluation*, edited by Y. Bar-Cohen (The American Soceity for Nondestructive Testing Inc., 1999), p. 189.

29. M. Asai and Y. Suzuki, Mater Sci Forum **327-3**, p. 17 (2000).

30. M. T. Hutchings and A. D. Krawitz, *Measurement of Residual and Applied Stress using Neutron Diffraction*. (Kluwer Academic, The Netherlands, 1992).

31. M. A. M. Bourke, R. Vaidyanathan and D. C. Dunand, Appl. Phys. Lett. **69** (17), p. 2477 (1996).

32. R. Vaidyanathan, M. A. M. Bourke and D. C. Dunand, J. Appl. Phys. **86** (6), p. 3020 (1999).

33. R. Vaidyanathan, M. A. M. Bourke and D. C. Dunand, Acta Mater. **47** (12), p. 3353 (1999).

34. R. Vaidyanathan, D. C. Dunand and U. Ramamurty, Mater. Sci. Eng. A **289**, p. 208 (2000).

35. C. R. Rathod, A. Little, D. W. Brown, M. A. M. Bourke and R. Vaidyanathan, Acta Mater. (To be submitted), (2005).

36. A. C. Larson and R. B. V. Dreele, Report No. LAUR 8-748, Los Alamos National Laboratory, (1986).

37. K. Gall, M. L. Dunn, Y. Liu, P. Labossiere, H. Sehitoglu and Y. I. Chumlyakov, Trans. ASME **124**, p. 238 (2002).

38. K. Gall, K. Juntunen, H. J. Maier, H. Sehitoglu and Y. I. Chumlyakov, Acta Mater. **49**, p. 3205 (2001).

39. N. Wangyang, Y. T. Cheng and D. S Grummon, Appl. Phys. Lett. **80** (18), p. 3310 (2002).

40. N. Wangyang, Y. T. Cheng and D. S. Grummon, Surf. Coat. Technol. **177**, p. 512 (2004).

41. D. C. Dunand, D. Mari, M. A. M. Bourke and J. A. Roberts, Metall. Mater. Trans. A **27** (9), p. 2820 (1996).

42. D. E. Hodgson, M. H. Wu and R. J. Biermann, in *Properties and Selection: Nonferrous Alloys and Special-Purpose Materials* (ASM International, Ohio, 1990), Vol. 2, p. 897.

43. Y. Liu and H. Xiang, J. Alloy. Compd. **270** (1-2), p. 154 (1998).

44. K. L. Johnson, *Contact Mechanics*. (Cambridge University Press, Cambridge, 1985).

45. R. Liu, D. Y. Li, Y. S. Xie, R. Llewellyn and H. M. Hawthorne, Scripta Mater. **41** (7), p. 691 (1999).

46. K. Otsuka and X. Ren, Prog. Mater. Sci. **50**, p. 511 (2005).

47. L. E. Goodman and L. M. Keer, Int. J. Solids Struct. **1**, p. 407 (1965).

48. ABAQUS Finite Element Analysis Program (ABAQUS Inc., Pawtucket. RI, 2004).

49. S. Suresh, J. Alcala and A. E. Giannakopoulos, US Patent No. 6134954 (2000).

50. K. Otsuka and C. M. Wayman, *Shape Memory Mateirals*. (Cambridge University Press, Cambridge, 1998).

51. F. X. Gil, J. M. Manero and J. A. Planell, J. Mater. Sci.-Mater. M. **7**, p. 403 (1996).

52. K. N. Melton and O. Mercier, Acta Metall. Mater. **27** (1), p. 137 (1979).

53. S. Miyazaki, T. Imai, K. Otsuka and Y. Suzuki, Scripta Metall. Mater. **15** (8), p. 853 (1981).

54. S. Miyazaki, T. Imai, Y. Igo and K. Otsuka, Metall Trans A **17** (1), p. 115 (1986).

55. M. Kawaguchi, Y. Ohashi and H. Tobushi, JSME Int. J. **34** (1), p. 76 (1991).

56. H. Tobushi, H. Iwanaga, K. Tanaka, T. Hori and T. Sawada, JSME Int. J. **35** (3), p. 271 (1992).

57. R. Vaidyanathan, M. A. M. Bourke and D. C. Dunand, Metall. Mater. Trans. A **32** (3A), p. 777 (2001).

58. Wangyang Ni, Yang -Tse Cheng and David S. Grummon, Surface and Coatings Technology **177-178**, p. 512 (2004).

59. X. -G. Ma and K. Komvopoulos, Appl. Phys. Lett. **83** (18), p. 3773 (2003).

60. B. I. Yakobson, C. J. Brabec and J. Bernholc, Phys. Rev. Lett. **76**, p. 2511 (1996).

61. L. G. Van, C. V. Alsenoy, V. V. Doren and P. Geerlings, Chem. Phys. Lett. **326**, p. 181 (2000).

62. M. M. Treacy, T. W. Ebbesen and J. M. Gibson, Nature **381**, p. 678 (1996).

63. O. Lourie and T. W. Wagner, J. Mater. Res. **13**, p. 2418 (1998).

64. M. Yu, O. Lourie, M. J. Dyer, K. Moloni, T. F. Kelly and R. S. Ruoff, Science **287**, p. 637 (2000).

65. M. Yu, B. S. Files, S. Arepalli and R. S. Ruoff, Phys. Rev. Lett. **84**, p. 5552 (2000).

66. N. Hamada, S. Sawada and A. Oshiyama, Phys. Rev. Lett. **68** (10), p. 1579 (1992).

67. H. Dai, J. Kong, C. Zhou, N. Franklin, T. Tombler, A. Cassel, S. Fan and M. Chapline, J. Phys. Chem. B **103**, p. 11246 (1999).

68. Y. Fu, W. Huang, H. Du, X. Huang, J. Tan and X. Gao, Surf. Coat. Technol. **145** (1-3), p. 107 (2001).

69. G. A. Shaw, D. S. Stone, A. D. Johnson, A. B. Ellis and W. C. Crone, Appl. Phys. Lett. **83** (2), p. 257 (2003).

70. C. P. Frick, A. M. Ortega, J. Tyber, K. Gall and H. J. Maier, Metall. Mater. Trans. A **35A** (7), p. 2013 (2004).